

Characterization of the Simulated Regional Snow Albedo Feedback Using a Regional Climate Model over Complex Terrain

THEODORE W. LETCHER AND JUSTIN R. MINDER

University at Albany, State University of New York, Albany, New York

(Manuscript received 3 March 2015, in final form 25 June 2015)

ABSTRACT

Midlatitude mountain regions are particularly sensitive to climate change because of an active snow albedo feedback (SAF). Here, the SAF is characterized and quantified over the complex terrain of the Colorado Headwaters region using high-resolution regional climate model simulations. A pair of 7-yr control and pseudo-global warming simulations is used to study the regional climate response to a large-scale thermodynamic climate perturbation. Warming is strongly enhanced in regions of snow loss by as much as 5°C. Linear feedback analysis is used to quantify the strength of the SAF within the Headwaters region. The strength of the SAF reaches a maximum value of $4 \text{ W m}^{-2} \text{ K}^{-1}$ during April when snow loss coincides with strong incoming solar radiation. Simulations using 4- and 12-km horizontal grid spacing show good agreement in the strength and timing of the SAF, whereas a 36-km simulation shows discrepancies that are tied to differences in snow accumulation and ablation caused by smoother terrain. Energy budget analysis shows that transport by atmospheric circulations acts as a negative feedback to regional warming, damping the effects of the SAF. On the mesoscale, the SAF nonlocally enhances warming in locations with no snow, and enhances snowmelt in locations that do not experience snow cover change. The methods presented here can be used generally to quantify the role of the SAF in simulated regional climate change, illuminating the causes of differences in climate warming between models and regions.

1. Introduction

Land regions with transient snow cover are particularly sensitive to climate change due to the snow albedo feedback (SAF). The SAF enhances warming through two physical processes: 1) as snow melts, the darker land surface underneath becomes more exposed, reducing the surface albedo; and 2) prior to melting, as the snowpack warms, the albedo of the snow itself decreases because of snow crystal metamorphosis and the concentration of light absorbing impurities within the snowpack. In both cases, the albedo reduction increases the surface absorption of shortwave (SW) radiation, resulting in surface heating that is conveyed through the lower troposphere via turbulent fluxes (e.g., [Randall et al. 1994](#)). Generally, the SAF is dominated by changes in snow cover, rather than snow

metamorphosis (e.g., [Qu and Hall 2007](#); [Fernandes et al. 2009](#)), except perhaps in regions where the snow is affected by impurities, for instance, dust or black carbon ([Fernandes et al. 2009](#)).

Midlatitude mountain ranges are especially susceptible to the SAF, as these regions often accumulate large snowpacks that persist through the late spring and into the summer when solar insolation is at its highest. This study is focused on the mountainous region of Colorado. The focus on this region stems, in part, from its societal importance, as it serves as the headwaters for many major river systems in the western United States. Throughout the paper, this region will be referred to as the Headwaters region (outlined in [Fig. 1](#)). On average, 70% of the annual runoff within the Headwaters region comes from high-elevation winter snowpack, making the snowpack in this region critical to the water resources in the western United States (e.g., [Christensen et al. 2004](#)). The seasonal snowpack also serves as the basis for the robust skiing and tourism industry. In the coming century, the snowpack in the western United States is expected to decrease significantly as the climate warms (e.g., [Christensen and Lettenmaier 2007](#); [Gao et al. 2011](#);

Corresponding author address: Theodore Letcher, Department of Atmospheric and Environmental Sciences, University at Albany, State University of New York, 1400 Washington Ave., Albany, NY 12222.
E-mail: tletcher@albany.edu

Klos et al. 2014). Many studies already show snowpack declines in the western United States due to warming (Mote et al. 2005; Kapnick and Hall 2012), that have been attributed in part to anthropogenic climate change (Pierce et al. 2008).

The SAF has been well studied in the global context, where typically it is considered as part of the total surface albedo feedback. Global estimates of the surface albedo feedback generally range between 0.2 and $0.8 \text{ W m}^{-2} \text{ K}^{-1}$ (e.g., Cess et al. 1991; Colman 2003; Soden et al. 2008; Qu and Hall 2014). This places the surface albedo feedback below the combined water vapor–lapse rate feedback in regards to global importance (e.g., Soden et al. 2008). Regionally, however, the surface albedo feedback can be dominant. For example, Qu and Hall (2014) and Taylor et al. (2007) show regional springtime maxima in SAF strength $>2 \text{ W m}^{-2} \text{ K}^{-1}$ throughout the Northern Hemisphere high latitudes, and over all of the significant midlatitude mountain ranges, including the Colorado Rockies. Fyfe and Flato (1999) ran global climate model (GCM) simulations, at approximately $3.75^\circ \times 3.75^\circ$ horizontal grid spacing, to study climate change over the Colorado Rockies and found regionally enhanced warming coincident with changes in snow cover that was as high as 4°C that they attributed to the SAF.

However, estimates of the SAF by GCMs over mountain ranges should be met with skepticism as topography has profound effects on patterns of precipitation, temperature, and snow that cannot be captured by GCMs. In particular, coarse-resolution models have been shown to perform poorly with respect to temperature and precipitation over complex terrain (Mass et al. 2002; Leung and Qian 2003; Ikeda et al. 2010; Rasmussen et al. 2011). Furthermore, any mesoscale features of the SAF in these regions are not resolved at all by GCMs, so its regional climate effects are unclear.

Recently, regional climate downscaling experiments using regional climate models (RCMs) have been used to investigate climate change in mountain regions. Several of these point to the SAF as a significant mesoscale feature of mountain climate change, responsible for regional variability in climate change and elevation dependent warming (e.g., Giorgi et al. 1997; Fyfe and Flato 1999; Salathé et al. 2008; Kotlarski et al. 2012). For example, Salathé et al. (2008) investigated regional climate change over the mountains of the northwest United States. In comparing the warming between their RCM and its parent GCM, they found increased warming (locally greater than 1.5°C) in the RCM spatially correlated with snow loss. These results provide evidence that over complex terrain the SAF strongly

modulates climate warming in ways that are poorly captured by GCM experiments.

Regional snow loss, exacerbated by the SAF may also be important to summertime temperature and precipitation, as the earlier spring runoff and additional warming caused by snow loss can lead to a local decrease in soil moisture that persists through the summer, thus increasing temperature and decreasing precipitation (e.g., Hall et al. 2008; Im et al. 2010). The SAF in the Headwaters region is further complicated by the effect of snow impurities, in particular dust, that locally can lower the snow albedo by as much as 15% and enhance snowmelt (Painter et al. 2007; Qian et al. 2011; Oaida et al. 2015).

Overall, previous research suggests that the SAF is important in amplifying climate change over midlatitude mountain regions, yet, a thorough quantitative analysis of the SAF over complex terrain has not been performed using RCM output.

In this study we use output from the Weather Research and Forecast (WRF) Model configured as a high-resolution RCM to investigate the SAF over the mountains of Colorado. Key questions we address in this study include the following: 1) How can the SAF be quantified using RCM output? 2) How does the SAF vary spatially, diurnally, and seasonally over complex terrain? 3) How does the RCM-simulated SAF depend on model resolution? 4) What are the nonlocal effects of the regional SAF associated with regional energy transport? To address these questions, the paper will be structured as follows. In section 2 we develop a framework to quantify the regional SAF over complex terrain based on linear feedback and energy budget analyses. In section 3 we use this framework to examine the seasonality of the SAF, its spatial structure, and its sensitivity to model resolution and region. This framework is also used to investigate nonlocal effects of the SAF. Sections 4 and 5 will discuss and summarize the results of this study.

2. Data and methods

a. WRF Model experiment

Here we use output from WRF RCM simulations described in Rasmussen et al. (2014) to examine the SAF. Figure 1 shows the full model domain centered over the Headwaters region, which is the focus of our analysis. These simulations were run at three different horizontal grid spacings: $\Delta x = 4 \text{ km}$, 12 km , and 36 km . These resolutions are substantially higher compared to many current RCMs, for example the North American Regional Climate Change Assessment Program

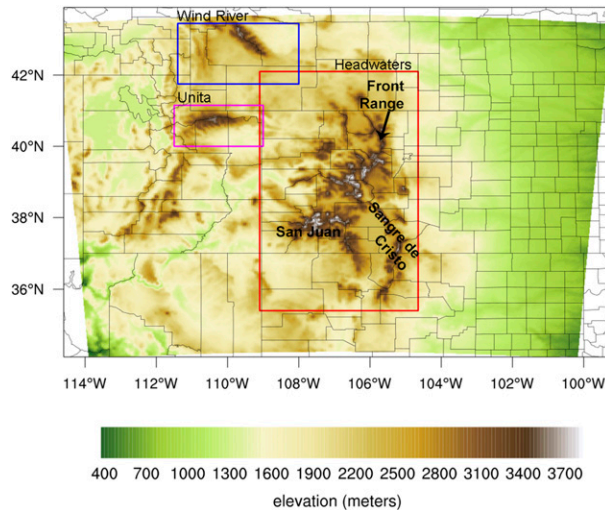


FIG. 1. Topography of the full WRF Model domain ($\Delta x = 4$ km).

(NARCCAP) models are run with 50-km grid spacing. The representation of the terrain for each of these grid spacings is compared to a high-resolution (0.008°) representation of the terrain, as well as the Community Climate System Model (CCSM3) GCM terrain (Fig. 2). At $\Delta x = 4$ km, most terrain features within the Headwaters domain are well resolved. At 12 km, the general topography of the region is still recognizable, however, the relief of individual mountain ranges and valleys is muted. At 36 km, relief is further reduced and various mountain ranges and valleys are completely eliminated (e.g., the Sangre de Cristo Mountains) such that the interior of the Headwaters region appears as a broad plateau. In CCSM3, the high terrain of the Headwaters region is represented by only three grid cells, which have elevation roughly 1 km lower than the actual mountain peaks.

The control simulations were run from October 2000 through October 2008. The North American Regional Reanalysis (NARR) was used to force the lateral boundaries every 3 hours. No grid nudging was applied within the WRF domain. A more detailed description of model setup can be found in Rasmussen et al. (2014). The simulated total precipitation showed good agreement with the observations from the Snowpack Telemetry (SNOTEL) network within the Headwaters region of Colorado (Rasmussen et al. 2014).

The pseudo-global warming (PGW) experimental framework (e.g., Schär et al. 1996) was used to test the regional climate response to large-scale climate change. The PGW approach applies an idealized climate perturbation to the control boundary forcing, rather than forcing the RCM boundaries with transient GCM output. Essentially, the PGW experiment provides boundary forcing with the same synoptic conditions as in the

control, only on a shifted base-state climate. The advantage of this approach is that it isolates the effects of large-scale warming and moistening from the effects of changes in midlatitude large-scale circulation and storm tracks. This allows us to examine how large-scale thermodynamic changes in climate interact with local mesoscale processes to shape regional climate. Because the natural variability of the large-scale flow is essentially identical between the control and PGW simulations, a regional analysis is possible over a shorter simulation period than is typically required for transient climate change experiments.

For the PGW experiment, GCM output from the CCSM3 model was used to perturb the boundary conditions (Rasmussen et al. 2014). The climate perturbation was taken to be the 10-yr monthly mean difference between 2045–55 and 1995–2005 from the CCSM3 ensemble mean using the Special Report on Emissions Scenarios (SRES) A2 emissions scenario (IPCC 2000). Perturbations were applied, at all vertical levels, to temperature, water vapor mixing ratio, geopotential height, and wind. The monthly mean perturbations were linearly interpolated in time and added to the NARR boundary conditions. In addition to the boundary forcing, a radiative perturbation consistent with an increase in CO_2 to 533 ppm (2050 concentrations from the A2 scenario) was applied as well. We only analyze model output starting in October 2001 to allow a full year for the land surface model (LSM) to adjust to the perturbed climate.

The Noah LSM (Koren et al. 1999; Chen and Dudhia 2001; Ek et al. 2003) was used in these simulations. The snow model component of Noah is highly simplified compared to the snow models used in several other common LSMs (Chen et al. 2014a). However, the simulations analyzed here were run with a version of Noah that includes recent improvements (Barlage et al. 2010). While Noah has four soil levels, it treats snow using a single vegetation-blended layer. Noah includes a variable snow density, fractional snow cover, and time-varying surface albedo. There is no explicit treatment of canopy interception.

In Noah, the surface albedo of a grid cell (α_s) is a linear combination of the snow albedo (α_{snow}) and the background snow-free surface albedo weighted by the fractional snow cover (f_{sn}). The term f_{sn} ranges from 0 to 1 and is an increasing function of snow water equivalent (SWE). The term α_{snow} decays with time according to the parameterization from Wigmosta et al. (1994):

$$\alpha_{\text{snow}}(t) = \alpha_{\text{snow, fresh}} A^{Bt}. \quad (1)$$

The empirically derived coefficients A and B are equal to 0.94 (0.82) and 0.58 (0.46), respectively, during the

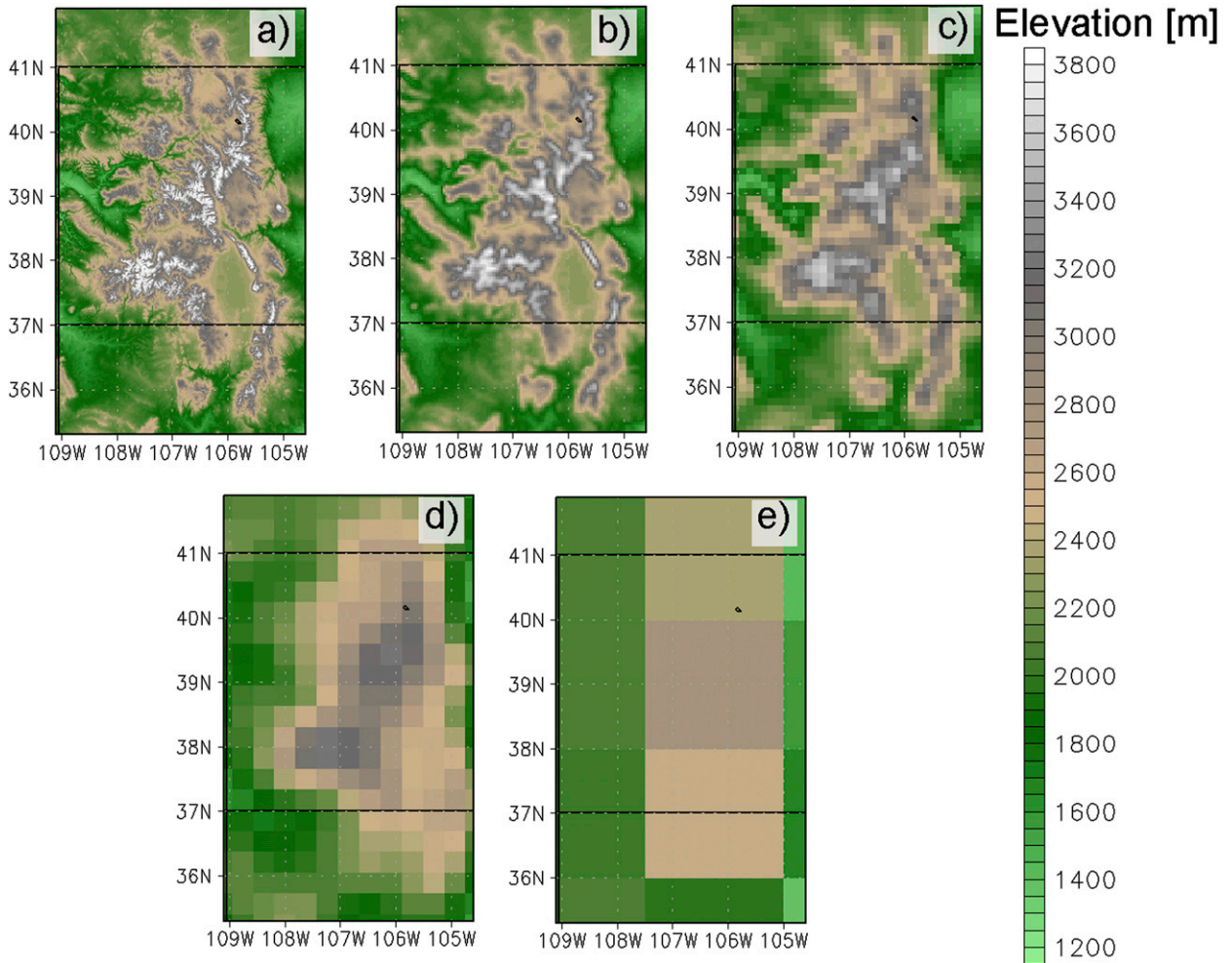


FIG. 2. Topography of the Headwaters region for varying model resolution. (a) High-resolution topography (0.008°), (b) WRF $\Delta x = 4$ km, (c) WRF $\Delta x = 12$ km, (d) WRF $\Delta x = 36$ km, and (e) CCSM3 $2.0^\circ \times 2.5^\circ$ grid.

accumulation (ablation) season. The term $\alpha_{\text{snow, fresh}}$ is the albedo of fresh snow, taken to be 0.85. The variable t is time in days since the most recent snowfall.

This version of Noah has shown good skill simulating SWE throughout the winter and early spring months in the Headwaters domain. The simulated SWE compares very well to SNOTEL observations during the early accumulation season, but is too low during the beginning of the snow ablation season (Barlage et al. 2010; Rasmussen et al. 2014). The timing of peak SWE in Noah agrees well with SNOTEL observations, however, the ablation season lasts too long, with simulated SWE persisting well past its observed disappearance (Chen et al. 2014b; Rasmussen et al. 2014). Recent work also indicates that Noah also tends to overestimate f_{sn} for high-resolution simulations over mountainous terrain (Wrzesien et al. 2015). Noah has no explicit representation of snowpack impurities such as dust or black carbon, which appear to

strongly affect snowmelt in portions of the Headwaters domain (Painter et al. 2007, 2010). These deficiencies in the Noah LSM add uncertainty to our results.

b. Linear feedback analysis

Linear feedback analysis is an effective method to quantify how radiative perturbations to Earth's energy budget are amplified or damped by various components of the climate system (e.g., Roe 2009). We use the framework described by Qu and Hall (2007) to quantify the strength of the SAF in the WRF simulations. In this framework the strength of the SAF is given by

$$\left(\frac{\partial Q}{\partial T_s}\right)_{\text{SAF}} = -Q_0 \frac{\Delta \alpha_s}{\Delta T_s} \frac{\partial \alpha_p}{\partial \alpha_s}. \quad (2)$$

The term on the left-hand side of Eq. (2) represents the change in net top of atmosphere (TOA) solar

radiative flux density (Q) per change in surface (2 m air) temperature (T_s) caused by changes in surface albedo (α_s) (and is given in units of $\text{W m}^{-2} \text{K}^{-1}$). The first term on the right-hand side, Q_0 , is the incoming solar radiation at TOA. The second term is the change in α_s over the change in T_s , differenced between two climate states. This term represents the dependence of α_s on T_s . The third term is the partial derivative of planetary albedo (α_p) with respect to α_s . This term accounts for the two-way attenuation of shortwave radiation as it passes through the atmosphere. For instance, α_p will be more affected by a change in α_s under clear-sky conditions than it will under cloudy conditions.

Equation (2) is used to quantify the SAF on monthly time scales, spatially averaged over the Headwaters domain. The second term is calculated by differencing the two climate states (PGW-control) then spatially averaging monthly mean values of $\Delta\alpha_s$ and ΔT_s over the Headwaters domain before taking their ratio. Thus, our analysis follows the definition of “local feedback analysis,” from [Feldl and Roe \(2013a\)](#), in that ΔT_s is averaged over the Headwaters domain, rather than over the entire globe. The applicability of linear feedback analysis is dependent on the linearity of the relationship between $\Delta\alpha_s$ and ΔT_s . We find a clear linear relationship between ΔT_s and $\Delta\alpha_s$ during the spring [March–June (MAMJ)] season ([Fig. 3](#)).

The third term cannot be calculated as a simple difference between climate states as it involves a partial derivative. There are a number of different methods used to calculate this term (e.g., [Taylor et al. 2007](#); [Qu and Hall 2007](#); [Donohoe and Battisti 2011](#)). We use the method described by [Donohoe and Battisti \(2011\)](#), which relies on a single-layer representation of the atmosphere. We chose this method as it is relatively simple to apply using standard WRF Model output, and because it has shown good agreement with more robust kernel methods ([Qu and Hall 2014](#)). To apply this method, $\partial\alpha_p/\partial\alpha_s$ is calculated at each grid cell using monthly mean values of the SW radiative fluxes and is then spatially averaged over the Headwaters domain. We use the value from the control simulation to avoid incorporating nonsurface related feedbacks (e.g., water vapor or clouds) into our analysis. However, a small decrease in $\partial\alpha_p/\partial\alpha_s$ (on average $< 5\%$) is found in the PGW simulation as compared to the control. The seasonality of this decrease correlates well with the seasonality of differences in cloud radiative forcing (CRF), so we speculate that this decrease is likely associated with changes in clouds. These changes represent a second-order interaction between various climate feedbacks, thus they are ignored in our linear feedback analysis.

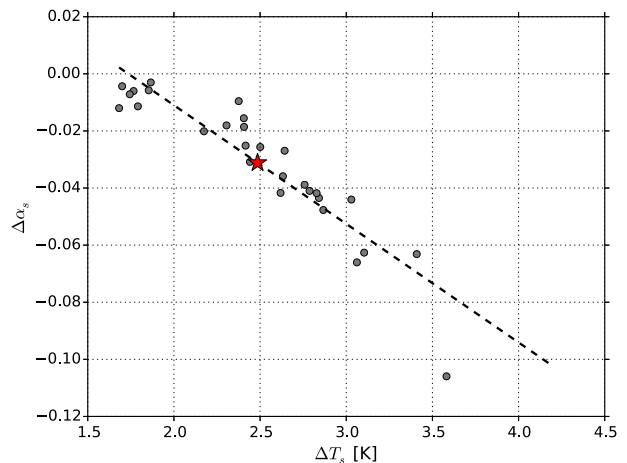


FIG. 3. Change in T_s vs α_s for March–June (MAMJ). Each point represents a single monthly mean value from a single year, averaged over the Headwaters domain. The dashed black line shows the linear regression line ($r = -0.91$, $p < 0.01$). The star shows the mean for MAMJ over the 7-yr dataset.

c. Energy budget formulation

To explore the nonlocal effects of the SAF, we use an energy budget analysis to quantify changes in horizontal energy transport in both the control and PGW simulations. In this framework, the total tropospheric energy budget is used:

$$\left(\frac{dE}{dt}\right) = \text{LW}_{\text{TOA}} + \text{SW}_{\text{TOA}} - F_{\text{sfc}} - \mathbf{V} \cdot \mathbf{F}. \quad (3)$$

Equation (3) is made up of the net TOA shortwave (SW_{TOA}) and net longwave (LW_{TOA}) radiative energy fluxes, the energy tendency of the troposphere (dE/dt), the surface energy flux (F_{sfc}), and the divergence of horizontal energy transport caused by atmospheric motions ($\mathbf{V} \cdot \mathbf{F}$). This equation is written such that positive values of the terms on the right-hand side represent sources of energy to the atmospheric column. The tropospheric integrated total energy is given by

$$E = -\frac{1}{g} \int_{p_{\text{top}}}^{p_{\text{sfc}}} (c_p T + L_v q + \Phi + k) dp, \quad (4)$$

and \mathbf{F} is the column-integrated horizontal energy transport:

$$\mathbf{F} = -\frac{1}{g} \int_{p_{\text{top}}}^{p_{\text{sfc}}} (c_p T + L_v q + \Phi + k) \mathbf{v} dp, \quad (5)$$

where \mathbf{v} is the horizontal wind vector. The term F_{sfc} is the energy exchange between the atmosphere and the

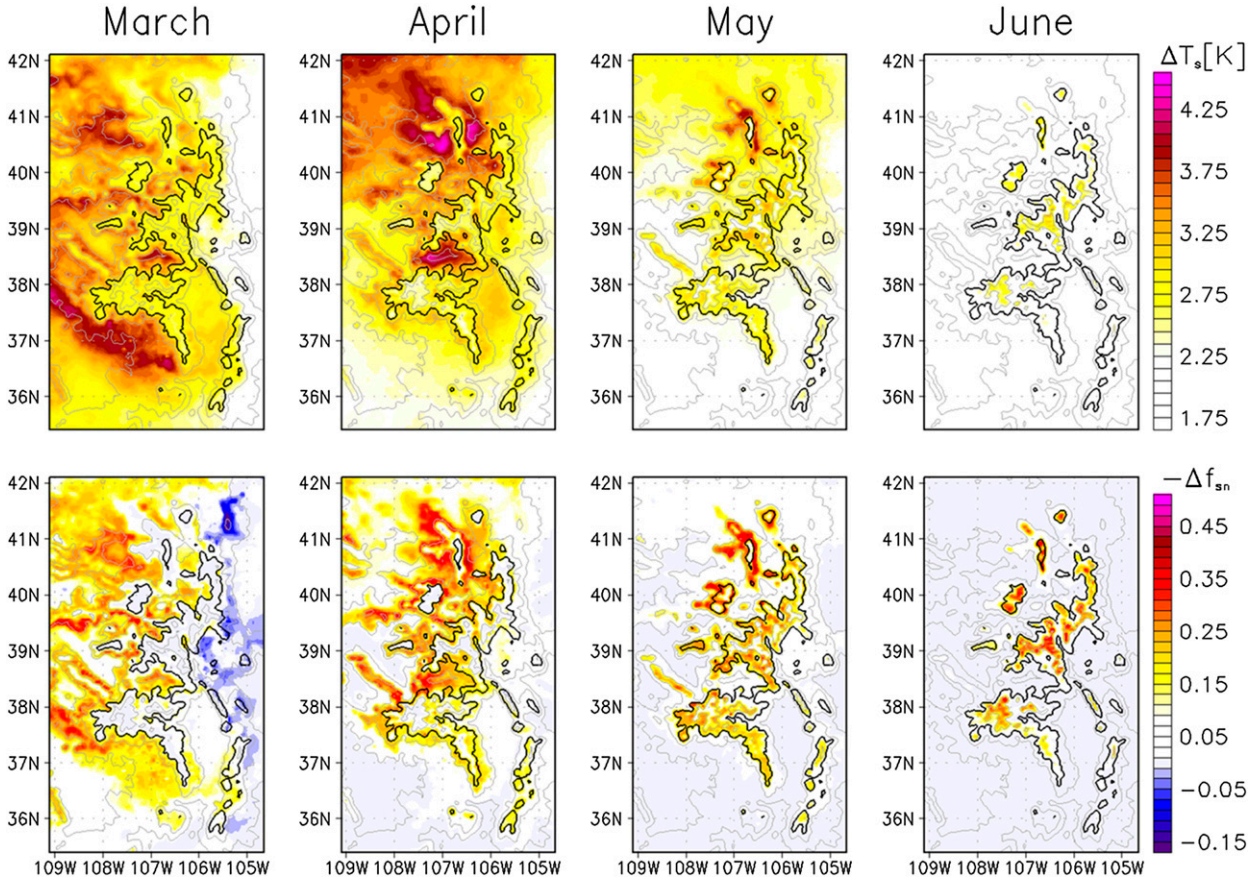


FIG. 4. Average (2002–08) pattern of warming and snow loss. (top) Temperature change (PGW-control) and (bottom) $-\Delta f_{\text{sn}}$ (PGW-control). The gray contours represent topography (500-m interval) and the 3000-m contour is indicated by the thick black line.

ground, made up of the surface radiative, and turbulent, sensible (SH) and latent (LE) heat fluxes:

$$F_{\text{sfc}} = \text{SW}_{\text{sfc}} + \text{LW}_{\text{sfc}} - \text{SH} - \text{LE}. \quad (6)$$

The surface energy budget represents a balance between the surface-atmospheric fluxes and the ground (G) and snowmelt (M) fluxes:

$$M + G = \text{SW}_{\text{sfc}} + \text{LW}_{\text{sfc}} - \text{SH} - \text{LE}. \quad (7)$$

To relate the SAF and horizontal energy transport to surface snowmelt and surface storage of energy we combine Eq. (3) with Eq. (7) to yield the following:

$$0 = \text{LW}_{\text{TOA}} + \text{SW}_{\text{TOA}} - \left(\frac{dE}{dt} \right)_{\text{atm}} - (M + G) - \mathbf{V} \cdot \mathbf{F}. \quad (8)$$

Monthly mean values of WRF output were used to calculate the energy budget terms at TOA and the surface. The energy tendency term (dE/dt) was calculated by differencing E on monthly time scales. Calculating

$\mathbf{V} \cdot \mathbf{F}$ explicitly is not practical because the WRF energy budget does not close using the available hourly output. Instead, horizontal energy transport is calculated as the residual of the remaining energy budget terms from Eq. (3) (following e.g., Trenberth et al. 2001; Porter et al. 2011). By design, the momentum equations used in WRF are both energy and mass conserving (Skamarock et al. 2008); therefore, it is expected that these residuals are small, however, any residual energy will be included in the calculated value of $\mathbf{V} \cdot \mathbf{F}$.

3. Results

a. Qualitative characterization of the SAF

We first characterize the SAF by examining spatial patterns in the changes of T_s and f_{sn} . Figure 4 shows the 7-yr mean difference of temperature and snow cover for March through June. The strongest warming anomalies are, for the most part, spatially coherent with changes in snow cover over the Headwaters domain, suggesting that the SAF dominates the mesoscale structure of

climate warming over the Headwaters region. In general, snow cover is most sensitive to warming along the margins of the snowpack where the control surface temperature is near 0°C (Nolin and Daly 2006; Minder et al. 2011; Klos et al. 2014). Accordingly, during March, enhanced warming is widespread over the low and middle elevations. As spring progresses, the enhanced warming is shifted to higher elevations, following the fractional snow loss. Enhanced warming at the highest elevations does not occur until June.

In general, regions of enhanced warming are broader than regions of snow loss, suggesting that the SAF is able to increase the temperature in areas where albedo is not changing. To quantify this nonlocal impact of the SAF, the Headwaters-domain-average warming at snow-free grid cells was compared to the domain-average fractional snow loss (Fig. 5). Snow-free grid cells are defined as grid cells with $f_{sn} < 0.05$ in the control simulation. In years and months when the total domain snow loss is high, the temperature change at snow-free grid cells is enhanced. The nonlocal effects of the SAF will be discussed further in section 3e.

To better examine the effect of the SAF on the Headwaters region as a whole, we consider the seasonal cycle of domain-averaged T_s and α_s (Figs. 6a,b) and how they change under PGW forcing (Figs. 6c,d). The thick black line in Fig. 6c, is representative of the large-scale forcing applied to the boundary conditions, and is given by averaging ΔT_s (over all years) on the lateral boundaries of the full model domain. From September to January, the regional temperature response closely follows the boundary warming in all years. In contrast, during March–May, the regional warming is substantially greater than the warming applied to the boundaries. This enhanced warming is coincident with decreases in α_s , suggesting an important contribution from the SAF. Furthermore, the interannual variability of the anomalous spring warming is large, and correlated with the variability of α_s and $\Delta\alpha_s$. Essentially, the SAF adds interannual variability to the climate response to a forcing that has no interannual variability, since it amplifies the boundary warming to varying degrees depending on the extent of seasonal snow cover.

One complicating factor in this analysis is that the PGW forcing is derived from GCM output. Thus, the boundary forcing potentially incorporates SAF-enhanced warming simulated by the parent GCM, making the WRF SAF an underestimate of the total SAF. The extent to which this affects our results is unclear; however, we only expect a substantial influence of the GCM SAF on the boundary forcing during early spring when snow cover and the SAF extend to low elevations.

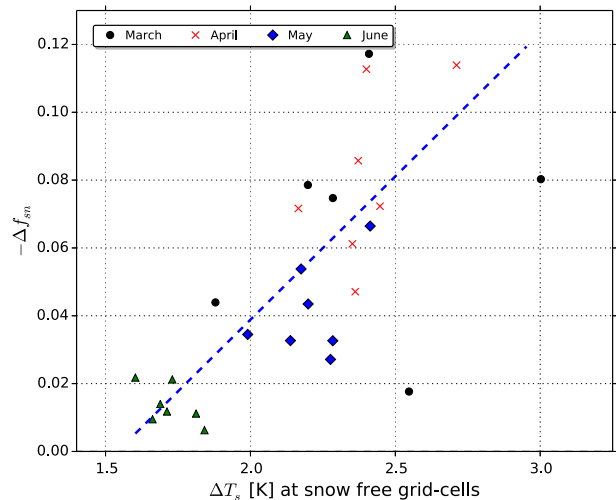


FIG. 5. The term Δf_{sn} averaged over the Headwaters domain vs ΔT_s at snow-free grid cells. Each point represents a singly monthly mean value of a single year. The included months are MAMJ. The linear regression is shown as the blue dashed line ($r = 0.7$, $p < 0.05$).

The excess warming during June–August is not associated with the SAF, as α_s does not change during this time. We speculate that changes in soil moisture or clouds play a role in this excess warming, though an analysis regarding the cause of the summertime regional warming is beyond the scope of this paper.

Figure 7 shows the detailed spatial structure of April mean snow cover and surface warming for two individual years, representing a warm/low-snowfall year (2007) and cold/high-snowfall year (2008). In April 2007, snow cover was limited to the highest terrain within the Headwaters domain. In contrast, the April 2008 snow cover was widespread over most of the northern Headwaters domain. The spatial patterns of warming for each year reflect the differences in snow cover. In April 2007, there is very little enhanced warming within the Headwaters domain, and the warming occurs at high elevations only, on the snow cover margins. More substantial warming occurs northwest of the Headwaters region, in southwest Wyoming where a large area of partial snow cover is present in the control simulation. In April 2008, there is much more warming within the Headwaters domain, consistent with the larger snow-covered area.

To characterize the vertical structure of SAF-enhanced warming, vertical cross sections of ΔT are plotted along the dashed lines of Fig. 7 (Figs. 8a,b). The monthly mean vertical profile of temperature change [$\Delta T(z)$] averaged along the lateral boundaries of the model domain was removed to separate local warming

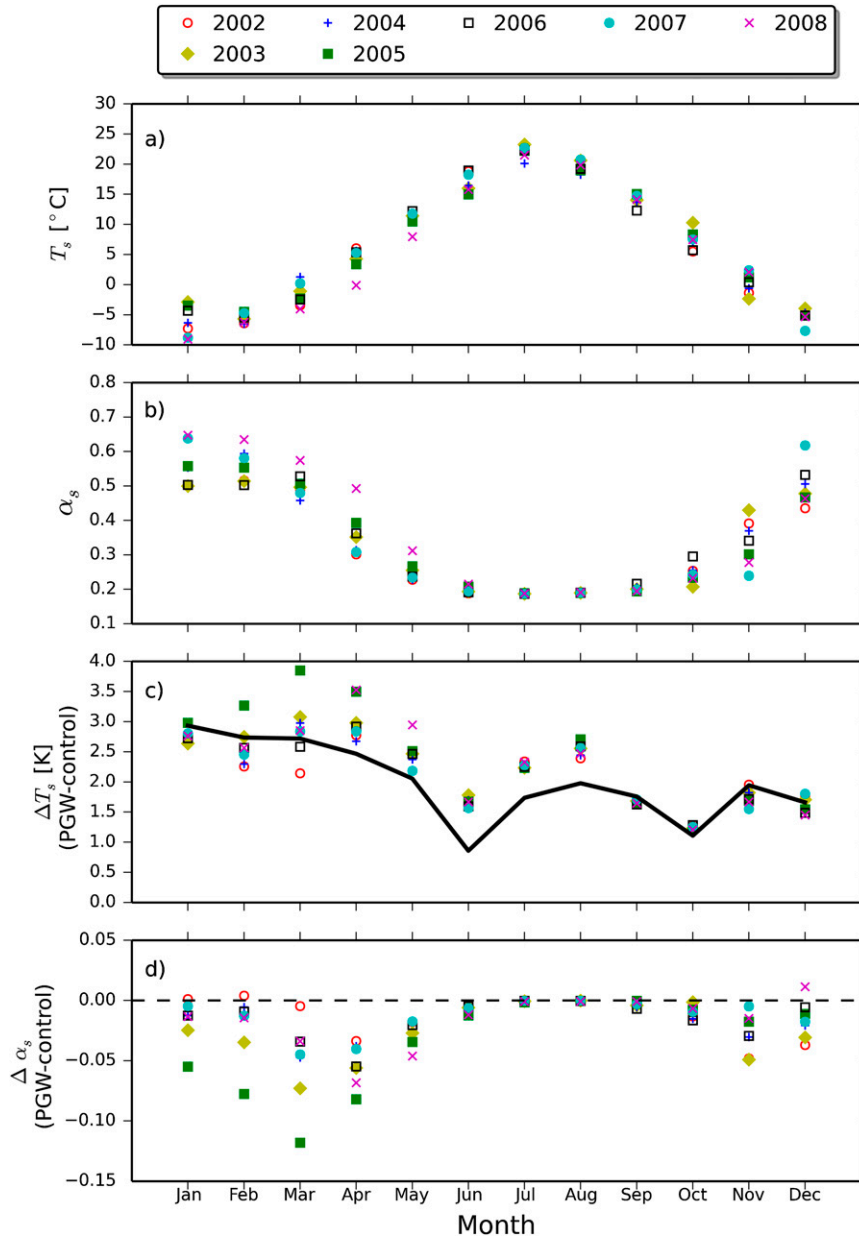


FIG. 6. Headwaters-domain averages of (a) T_s , (b) α_s , (c) ΔT_s (PGW-control), and (d) $\Delta \alpha_s$ (PGW-control). The thick black line in (c) shows ΔT_s on the model boundaries. Each point represents a different year as indicated by the key.

$[\Delta T'(z)]$ from the warming applied to the model boundaries. The fractional snow loss along this cross section is shown in Figs. 8c,d. In both years, the SAF-enhanced warming is mainly confined to the boundary layer, below 1 km AGL, and is strongest in regions of snow loss. Enhanced warming shows greater vertical extent in the vicinity of steep terrain, where vertical motions and turbulent mixing are likely, on average, stronger (e.g., increased gravity wave activity or

convection) facilitating greater air exchange between the free troposphere and the boundary layer.

To investigate the diurnal variability of the SAF, spatial patterns of monthly mean warming during April 2008 at 0400 LST (1200 UTC) and 1600 LST (0000 UTC) were examined (Fig. 9). There is notable diurnal structure in the SAF. Not only is the SAF-enhanced warming substantially stronger at 1600 LST, the spatial pattern in the warming is also different. At 1600 LST, localized

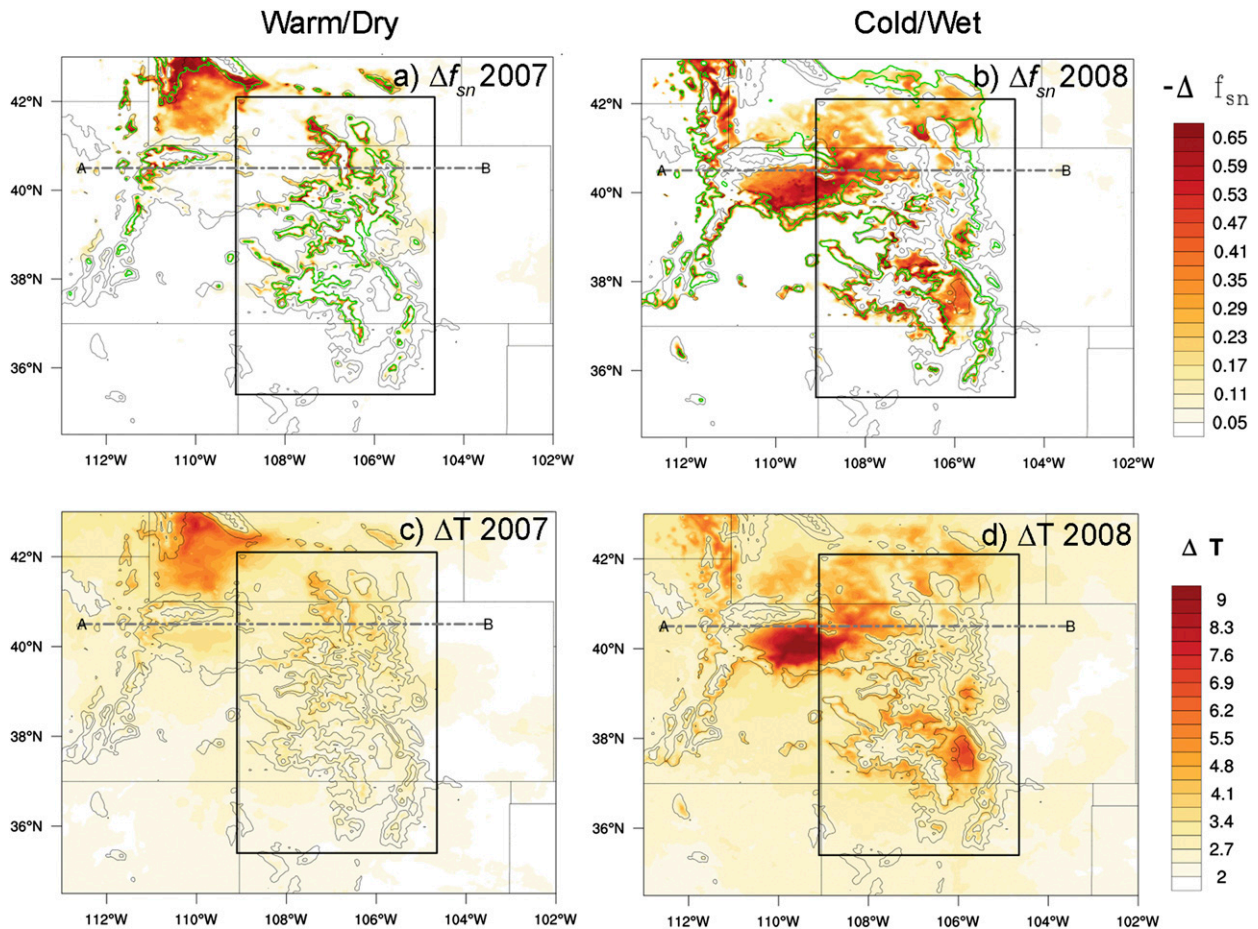


FIG. 7. April monthly mean snow cover and temperature change (PGW-control). The term Δf_{sn} for (a) 2007 and (b) 2008. The term ΔT_s for (c) 2007 and (d) 2008. The solid green line shows $f_{sn} = 0.65$ from the control simulation, and is representative of the snow cover edge. The gray contours represent topography (500-m interval).

strong warming occurs mainly along the lower slopes of prominent mountains and in high-altitude basins where snow cover is changing. At 0400 LST, the strongest warming is located in the valleys and basins within the Headwaters domain and there is less enhanced warming along mountain slopes. In some areas, the warming at 0400 LST is greater than the warming at 1600 LST. This is most notable in the area northwest of the Headwaters region. The diurnally dependent warming patterns suggest that topographically driven flows and cold air pools influence regional patterns of SAF-enhanced warming.

b. Linear feedback analysis: Seasonal and regional variability of the SAF

To better quantify the SAF and its variability, linear feedback analysis was applied to the Headwaters domain. The values of each term in Eq. (2) are in green in Fig. 10. These values are spatially averaged over the Headwaters domain and temporally averaged over the full 7-yr period

for each month. The whiskers represent interannual variability (10th–90th percentile). There are two peaks in $\Delta\alpha_s/\Delta T_s$: one in the spring and one in the fall. During the spring and fall, T_s is near 0°C , so warming affects both the precipitation phase and the rate of snow ablation, thus snow cover is sensitive to warming at these times. During winter, T_s is often well below 0°C , so the snow cover is largely unaffected by warming. During the summer, there is minimal snow, so $\Delta\alpha_s/\Delta T_s$ is nearly zero. The $\partial\alpha_p/\partial\alpha_s$ term has both low interannual and interseasonal variability. However, this term decreases slightly during the late fall and winter, likely due to increased regional cloudiness.

Figure 10d shows the magnitude of the SAF, $(dQ/dT_s)_{SAF}$, the product of the terms shown in Figs. 10a–c. The phasing of incoming solar radiation and $\Delta\alpha_s/\Delta T_s$ is critical to modulating the strength of the SAF. Low Q_0 in the fall results in a SAF that is greatly diminished compared to the spring despite similar values of $\Delta\alpha_s/\Delta T_s$. A

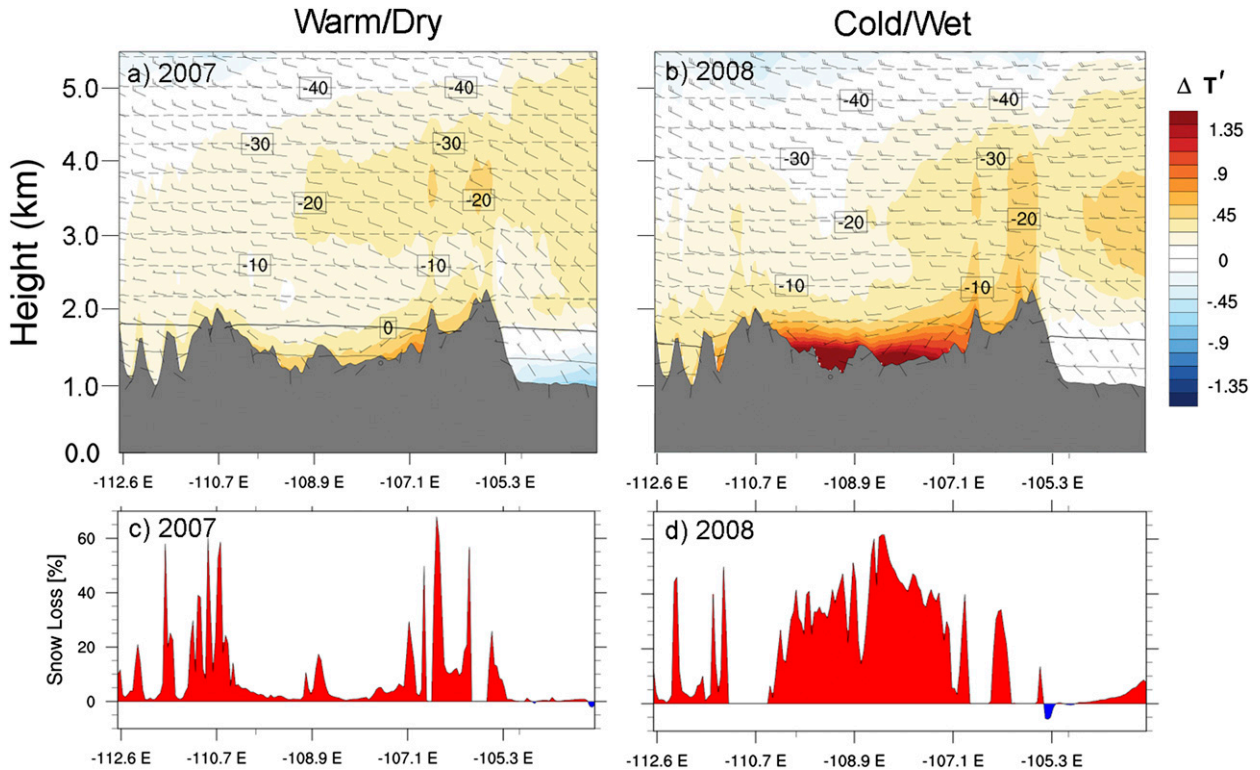


FIG. 8. April monthly mean cross sections along line (a)–(b) from Fig. 7. Vertical cross section of $\Delta T'$ for (a) 2007 and (b) 2008, where $\Delta T'$ is ΔT minus ΔT averaged on the lateral boundaries of the model domain. The dashed lines show the temperature from the control simulation, the wind barbs show the horizontal wind, and below-ground elevations are shaded. The term $-\Delta f_{sn}$ is shown for (c) 2007 and (d) 2008.

slightly lower $\partial\alpha_p/\partial\alpha_s$ is a smaller contribution to the diminished fall SAF. On average, the SAF reaches a peak strength in April of about $4 \text{ W m}^{-2} \text{ K}^{-1}$ and then slowly tails off into the late spring with decreasing snow cover.

The interannual variability in the SAF is quite high, particularly in March. During the late spring and early summer, the variability in SAF strength collapses. The high variability of the SAF during the early spring can be explained by the variability in snow cover at low-elevation areas within the domain (e.g., Figs. 6 and 7). High-snowfall years generally have a stronger SAF than low-snowfall years: the February–June (FMAMJ) mean control snow fraction is well correlated with the FMAMJ mean $(dQ/dT_s)_{\text{SAF}}$ ($r = 0.75$, $p < 0.05$). This is because during high-snowfall years there is more snow cover at low elevations, and thus a higher potential for the SAF to be active over a broader area. Additionally, in high-snowfall years, widespread snow loss occurs later in the spring and is thus coincident with high Q_0 .

The SAF for two other mountain regions within the full model domain was calculated for comparison: the Wind River Mountains in west-central Wyoming and the Uinta Mountain Range in northern Utah (Fig. 1). The seasonal cycle of the SAF in each of these regions shows similarities to the Headwaters seasonal cycle (Fig. 10). Both regions

show spring and fall peaks in the SAF, with a dominant spring peak in April. They have a stronger SAF during the spring and a weaker SAF during winter than the Headwaters region, likely because the Headwaters region includes more low-elevation grid cells that do not hold snow into the late spring and early summer.

Interestingly, while the mean SAF was slightly positive during the late winter, in some years this term was negative. The negative sign of the SAF is associated with a positive correlation between T_s and α_s . In general, precipitation is increased in the PGW simulation, primarily due to higher water vapor content (Rasmussen et al. 2011, 2014). During midwinter, the increased precipitation is more likely to come in the form of increased snowfall, as the warming is not strong enough to change the precipitation phase during this time. As such, temperature and albedo can sometimes exhibit a positive relationship if temperature-induced snowfall increases overwhelm temperature-induced increases in snow ablation and rain versus snow.

c. Linear feedback analysis: Sensitivity to model resolution

To investigate the sensitivity of SAF strength to model resolution, linear feedback analysis was applied

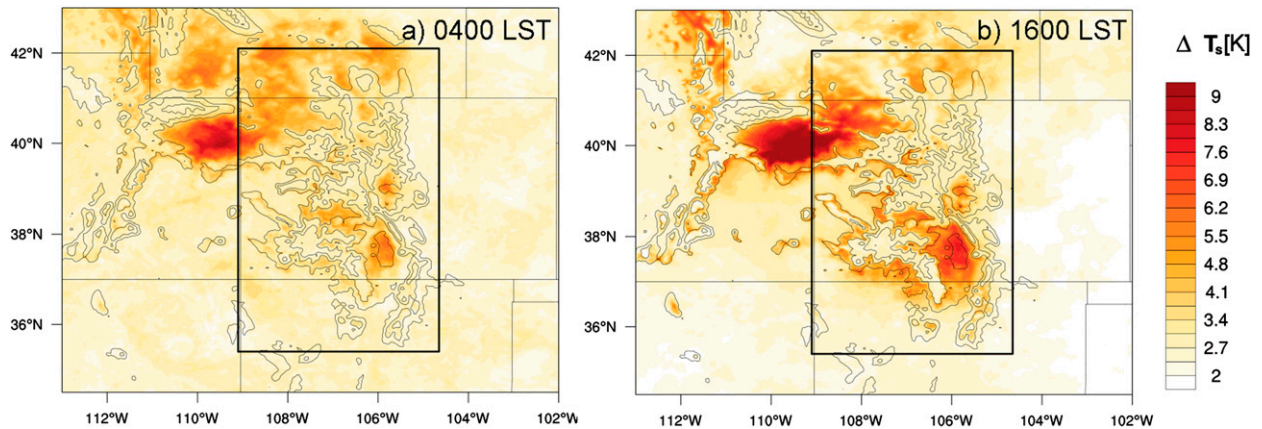


FIG. 9. Diurnal variation of April 2008 mean ΔT_s (PGW-control). (a) 0400 LST (1200 UTC) and (b) 1600 LST (0000 UTC). Contours represent topography (500-m interval). The Headwaters domain is outlined in black.

to simulations using the three grid spacings ($\Delta x = 4$ km, 12 km, and 36 km), limited to spring months (January–June) over the Headwaters domain (Fig. 11). The January–June mean SAF is nearly identical at all three model resolutions, approximately $2.4 (\pm 0.1) \text{ W m}^{-2} \text{ K}^{-1}$. Additionally, all three simulations generally agree in the seasonal variations of the SAF. The 36-km simulation stands out as the most different, with a stronger peak SAF, but a more rapid decrease in SAF strength into the summer season. The contrast in $(dQ/dT_s)_{\text{SAF}}$ between the 36-km simulation and the higher-resolution simulations is caused primarily by differences in $\Delta\alpha_s/\Delta T_s$. This contrast increases throughout the late spring as the differences in $\Delta\alpha_s/\Delta T_s$ are amplified by increasing Q_0 .

To understand the causes of this resolution dependence, spatial patterns of warming and snow loss at $\Delta x = 4$ km and $\Delta x = 36$ km were investigated (Fig. 12). In April, the 36-km simulation shows much stronger warming and greater snow loss than the 4-km simulation. In particular, snow loss occurs over the high interior mountains at 36 km where snow cover does not change at 4 km (e.g., the interior San Juan Mountains and the northwest portion of the Headwaters domain). In June, enhanced warming and snow loss are limited to the highest peaks in the 4-km simulation, but are completely absent from the 36-km simulation.

To further understand the mechanisms by which terrain resolution affects the strength and timing of the SAF, we examined the resolution differences (4 km – 36 km) for April and June values of variables relevant to the SAF: terrain height, T_s , f_{SN} , SWE, and calendar year-to-date accumulated precipitation (Fig. 13). The differences in topography show how terrain relief is substantially decreased at 36 km. This reduction in the range of elevations within the Headwaters domain makes the regional climate more homogenous. In both April and June, the difference in T_s is strongly

negatively correlated with the difference in terrain elevation. In April there is a redistribution of precipitation from high to low elevations, relative to 4 km.

As a result of these differences, during April, snow is more sensitive to warming at $\Delta x = 36$ km, because 1) there are more snow-covered grid cells within the elevation range where T_s is likely to be near or above 0°C and 2) the highest terrain is substantially reduced causing precipitation to decrease and temperature to increase at high-elevation grid cells, which in turn reduces snow accumulation and hastens snow ablation. This helps explain why the SAF at 36 km is stronger in April. In contrast, the SAF at 36 km is weaker in June because snow is not present anywhere in the domain at this time, and thus snow cover does not change. The SAF is strong over a shorter period of time at 36 km because snow cover is sensitive to warming at both high- and low-elevation grid cells simultaneously. At 4 km, the SAF is spread out in time because the regional climate is more heterogeneous and snow cover at low-elevation grid cells is not sensitive to warming at the same time as at high-elevation grid cells. Averaging over the February–June period, when the SAF is most active, the 36- and 4-km simulations have similar values of $(dQ/dT_s)_{\text{SAF}}$; however, the agreement is the result of substantial compensating seasonal and spatial biases in the 36-km run.

Differences in the control climate and, hence, the SAF are much more modest between 4 km and 12 km, consistent with findings from previous studies examining resolution dependence of mesoscale model simulations over mountainous terrain (Mass et al. 2002; Ikeda et al. 2010). These results suggest that a 12-km horizontal resolution is sufficient to capture the regionally averaged SAF over the Headwaters domain; however, higher resolution is required to capture finer-scale structures and variability in SAF enhanced warming.

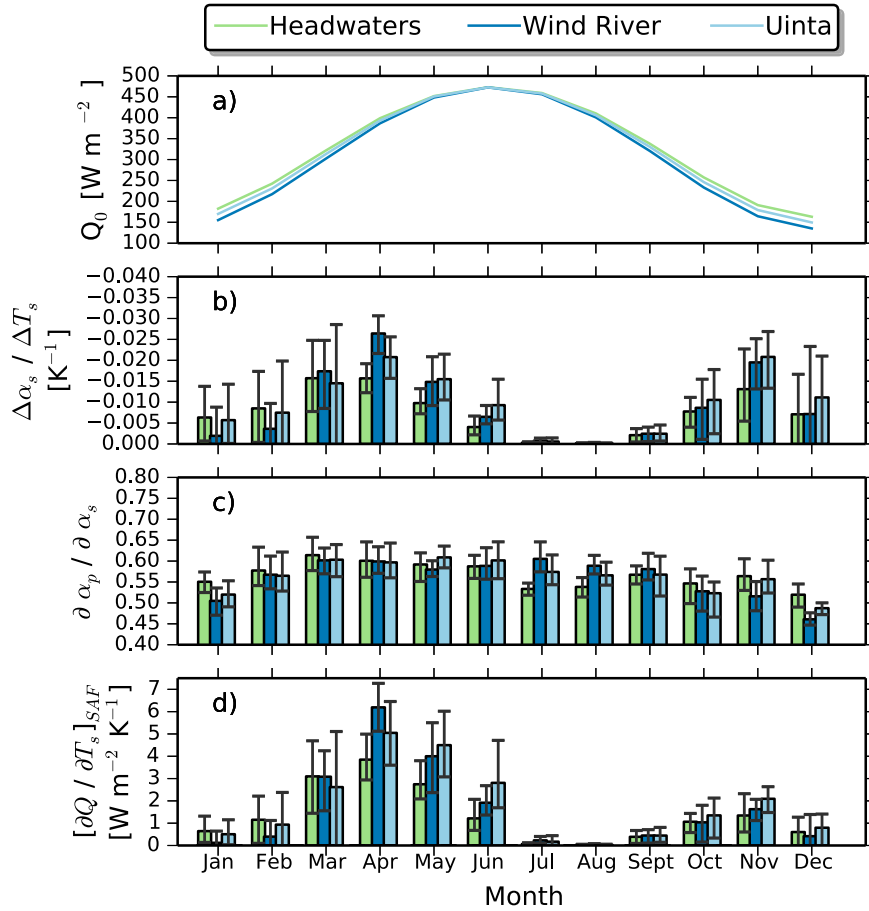


FIG. 10. Terms of the snow albedo feedback in Eq. (1), for the $\Delta x = 4$ km simulations: Headwaters, Wind River, and Uinta regions: (a) Q_0 , (b) $\Delta\alpha_s/\Delta T_s$, (c) $\partial\alpha_p/\partial\alpha_s$, and (d) $(\partial Q/\partial T_s)_{\text{SAF}}$. Whiskers show 10th–90th percentiles of interannual variability.

d. Estimating the SAF from the seasonal cycle of α_s and T_s

Our methods should be broadly useful for diagnosing the SAF in other RCMs. However, most RCM experiments do not include PGW-type simulations. For experiments without PGW output, the linear feedback framework can be used to calculate $\Delta\alpha_s/\Delta T_s$ by using seasonal variations in α_s and T_s (Hall and Qu 2006; Fletcher et al. 2012; Qu and Hall 2014). To estimate the SAF using this method, monthly mean values of α_s and T_s are differenced across adjacent months. Applying this method to the control output from WRF,¹ we find that the SAF calculated from seasonal cycle of α_s and T_s is able to reproduce the seasonality of the SAF as

well as the major differences in model resolution (Fig. 14). Furthermore, the strong correlation between the SAF calculated from the seasonal cycle and the SAF under the PGW experiment suggests that observationally based estimates of the SAF from the seasonal cycle could potentially be used to constrain the SAF in simulations of climate change (e.g., Fletcher et al. 2012).

e. Regional energy budget analysis: Nonlocal effects of the SAF

Here the energy budget framework described in section 2c is used to explore how SAF-enhanced warming is redistributed by horizontal energy transport caused by atmospheric circulations. Such energy transport may reduce the localized climate impact of the SAF, and allow the SAF to remotely cause warming in locations where snow cover does not change. The role of horizontal transport as it relates to climate feedbacks has been previously studied using

¹ In this analysis monthly mean values are centered at the beginning of each month, rather than in the middle, to make the seasonal $\Delta\alpha_s/\Delta T_s$ more directly comparable to the PGW $\Delta\alpha_s/\Delta T_s$.

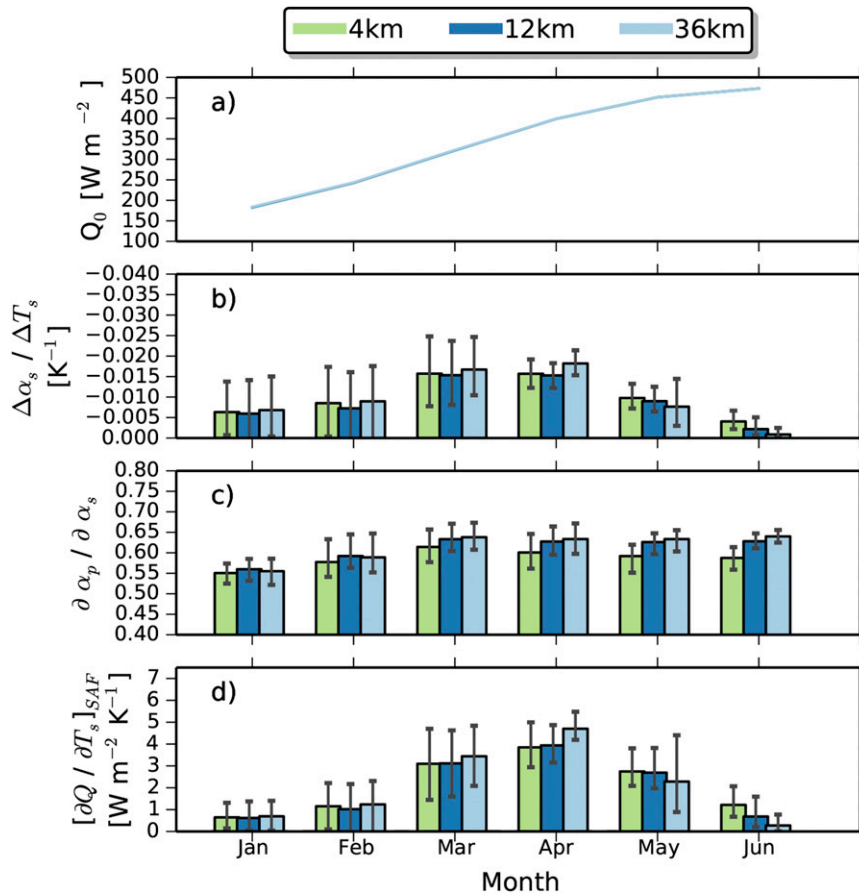


FIG. 11. Terms of the snow albedo feedback, for the Headwaters region at $\Delta x = 4$ km, 12 km, and 36 km: (a) Q_0 , (b) $\Delta\alpha_s/\Delta T_s$, (c) $\partial\alpha_p/\partial\alpha_s$, and (d) $(\partial Q/\partial T_s)_{\text{SAF}}$. Whiskers denote 10th–90th percentiles of interannual variability.

simplified global modeling experiments (e.g., Hall 2004; Feldl and Roe 2013b; Merlis 2014). On global scales, horizontal energy transport significantly dampens the local temperature response to feedbacks and enhances warming at locations remote from the feedback processes.

Monthly mean values of each of the terms of Eq. (8) were calculated and averaged over the 4-km Headwaters domain from January to June. Figure 15a shows the seasonality of the various terms. During the midwinter and early spring, energy is converged into the Headwaters region via transport, balancing the TOA radiative imbalance between the SW and longwave (LW) fluxes. As SW_{TOA} increases throughout the spring, ultimately changing the sign of the radiative imbalance, horizontal transport acts to export energy from the Headwaters domain.

To better understand the effects the SAF has on the domain mean energy balance, these terms were differenced between the PGW and control simulations (Fig. 15b).

The red line plotted in Fig. 15b is a measure of the radiative impact of the SAF attained by multiplying $(\partial Q/\partial T_s)_{\text{SAF}}$ by the Headwaters domain mean ΔT_s . In the energy budget, the SAF is manifest as a substantial increase in net SW_{TOA} , present from February to June. From January to May $\Delta\text{SW}_{\text{TOA}}$ is well correlated with SAF strength, though it is not as strong. In June $\Delta\text{SW}_{\text{TOA}}$ is stronger than the SAF. These differences between the magnitude of the SAF and $\Delta\text{SW}_{\text{TOA}}$ either indicate shortcomings of the linear feedback analysis or the presence of other feedbacks that act in addition to the SAF.

In the Headwaters domain, in March–May $\Delta\text{SW}_{\text{TOA}}$ is primarily balanced by increased energy transport out of the region [$\Delta(-\mathbf{V} \cdot \mathbf{F}) < 0$], rather than a regional increase in outgoing LW radiation ($\Delta\text{LW}_{\text{TOA}} < 0$) as would be expected in the absence of energy transport. There is a strong inverse linear relationship between $\Delta\text{SW}_{\text{TOA}}$ and $\Delta(-\mathbf{V} \cdot \mathbf{F})$ on both seasonal and interannual time scales (Fig. 16a). Here $\Delta(-\mathbf{V} \cdot \mathbf{F})$ is also

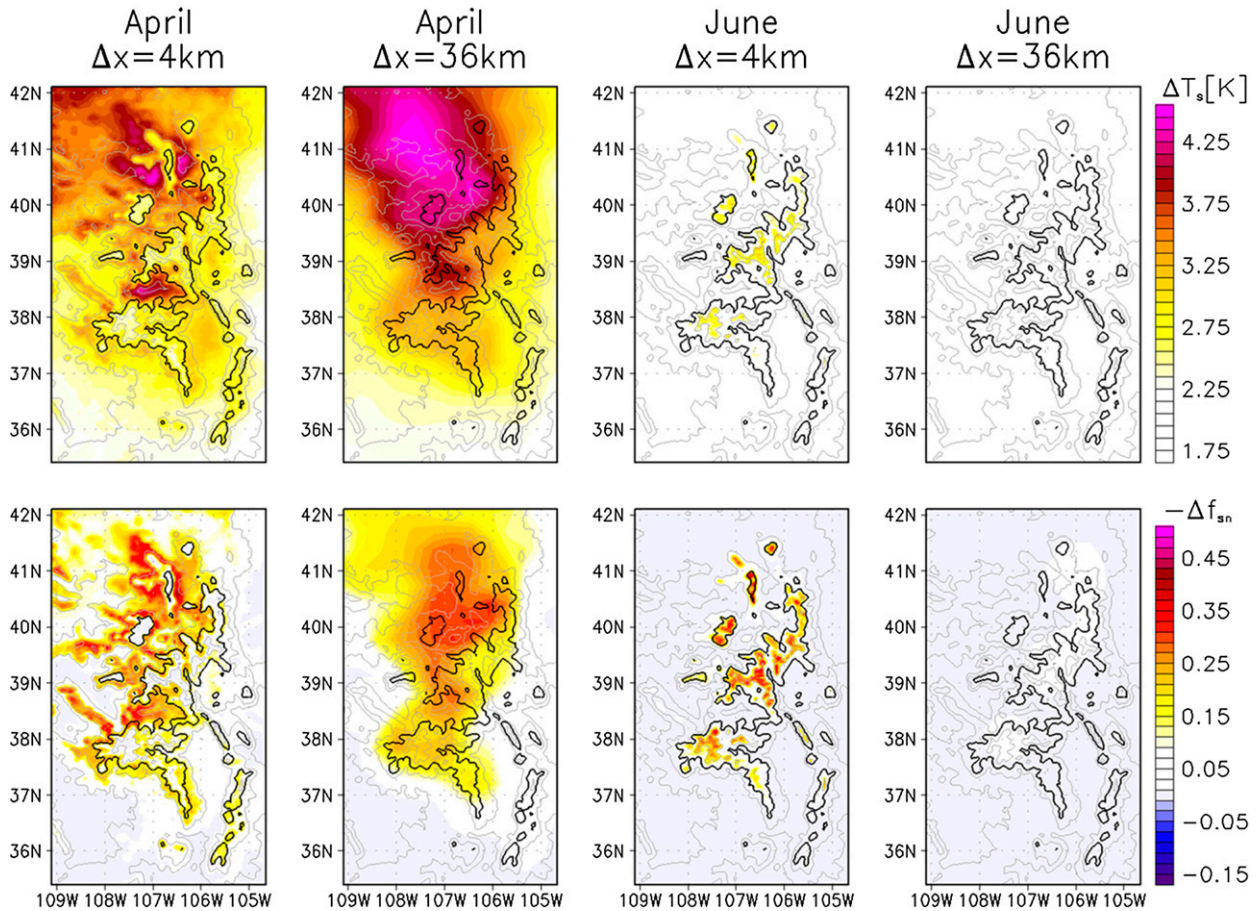


FIG. 12. Comparison of warming and snow loss between the $\Delta x = 4$ km and $\Delta x = 36$ km. (top) The 7-yr mean ΔT_s (PGW-control). (bottom) The 7-yr mean Δf_{sn} (PGW-control). The gray contours represent topography from the $\Delta x = 4$ km simulation (500-m interval) and the 3000-m contour is indicated by the thick black line.

proportional to the domain-averaged anomalous warming (Fig. 16b). These results indicate that heat transport acts as a negative feedback on regionally enhanced warming under climate change; in months when the SAF amplifies SW_{TOA} and local warming, anomalous heat transport increasingly acts to cool the region. In contrast, $\Delta \text{LW}_{\text{TOA}}$ is not well correlated with $\Delta \text{SW}_{\text{TOA}}$.

Changes in (dE/dt) , M , and G are small compared to changes in energy transport, however, the seasonality of ΔM is interesting. During March and April, ΔM is consistently negative, indicating that increased snowmelt within the Headwaters domain, contributes to balancing $\Delta \text{SW}_{\text{TOA}}$. During May and June, ΔM becomes positive as there is less snow available to melt in the PGW simulation.

To investigate the potential role of cloud feedbacks in the climate response, the TOA CRF was calculated. The CRF was calculated by differencing total and clear-sky TOA radiative fluxes:

$$\text{CRF} = (\text{LW}_{\text{TOA}} + \text{SW}_{\text{TOA}}) - (\text{LW}_{\text{TOA,clear}} + \text{SW}_{\text{TOA,clear}}). \quad (9)$$

Negative values of CRF imply a net cooling effect due to clouds, and positive values imply net warming. Figure 15c shows the change in CRF (PGW-control). From February to May, ΔCRF is negative. It is likely that some of ΔCRF is caused by decreases in α_s caused by snow loss, rather than by changes in clouds. Regardless, the sign of the ΔCRF indicates that the increase of clouds act to cool the region and cannot explain the positive $\Delta \text{SW}_{\text{TOA}}$ in February–May, although they may act to counteract the SAF and help explain the difference between $\Delta \text{SW}_{\text{TOA}}$ and $(\partial Q/\partial T_s)_{\text{SAF}}$. In contrast, during June there is a large positive ΔCRF along with minimal changes in α_s (Fig. 6d). Thus, it appears that in June $\Delta \text{SW}_{\text{TOA}}$ is dominated by cloud feedbacks, which explains why $\Delta \text{SW}_{\text{TOA}}$ exceeds what is expected from the SAF.

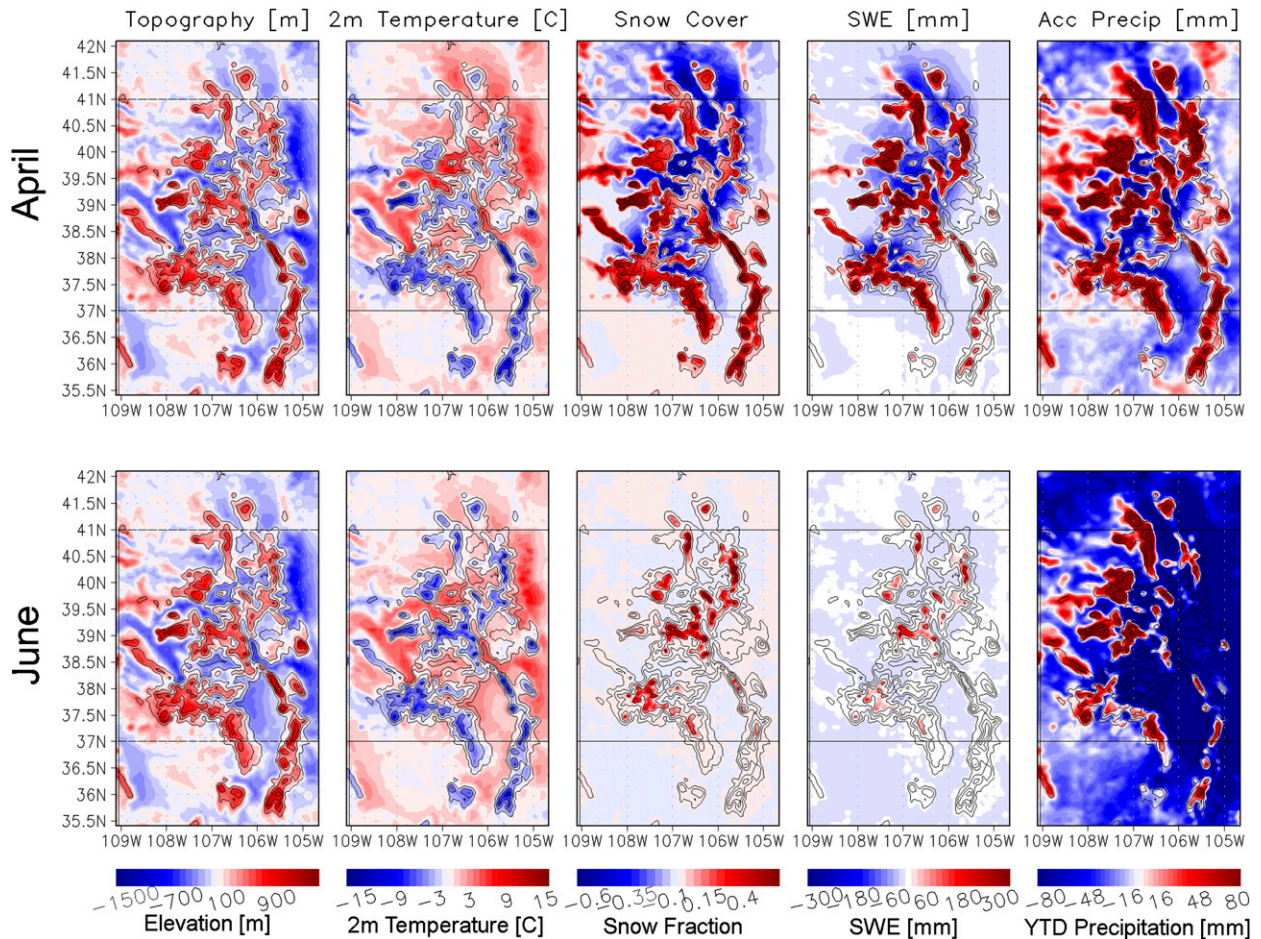


FIG. 13. Difference between control simulation results at different model resolutions (4 km – 36 km). (top) April and (bottom) June. Differences are for terrain elevation, T_s , f_{sn} , SWE, and year-to-date precipitation. Data are 7-yr averages.

To gain a better understanding of how changes in the energy budget terms relate to the regional terrain, spatial patterns of changes in the terms of Eq. (8) were investigated (Fig. 17). For this analysis, we focused on the San Juan Mountains in southwest Colorado, and used 7-yr means for April. The hatching in Fig. 17 indicates regions experiencing snow loss: $\Delta f_{sn} < -0.1$. The strong spatial coherence between $\Delta(\mathbf{V} \cdot \mathbf{F})$ and ΔSW_{TOA} (Figs. 16a,b) illustrates that locations with large albedo reductions due to snow loss are cooled by enhanced energy transport divergence. The magnitude of ΔLW_{TOA} (Fig. 16d) was small compared to $\Delta(\mathbf{V} \cdot \mathbf{F})$, and only slightly enhanced over snow-loss regions, demonstrating that energy transport dominates in balancing ΔSW_{TOA} .

Interestingly, there is substantial horizontal energy convergence [$\Delta(-\mathbf{V} \cdot \mathbf{F}) < 0$] over the interior San Juan Mountains, an area that was, on average, fully snow covered during April in both the control and PGW

climates. Because of the nature of the energy balance framework used, we cannot quantify how much of this energy convergence is caused by the SAF as opposed to large-scale forcing. Within these regions of energy convergence, ΔSW_{TOA} was negligible, indicating that the SAF was not active in these locations. Figure 16c shows that the increased energy convergence was balanced primary through the snowmelt at the surface. Multiplying ΔM by the latent heat of fusion gives melt rates as high as 3 mm day^{-1} in the fully snow-covered interior San Juan Mountains. This suggests that the SAF enhances snowmelt nonlocally via increased energy convergence over fully snow-covered areas.

4. Discussion

Figure 9 indicated substantial diurnal variability in the pattern of SAF-enhanced warming. This suggests that diurnally driven topographic flows redistribute

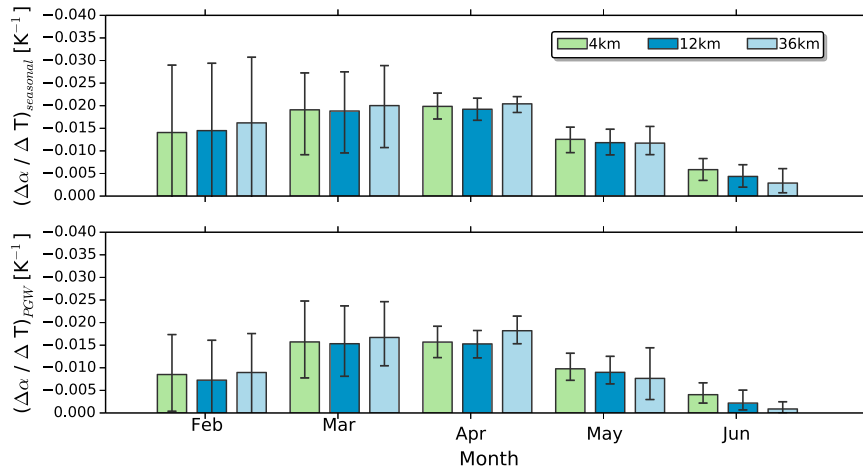


FIG. 14. Comparison between $(\Delta\alpha/\Delta T)_{\text{seasonal}}$ and $(\Delta\alpha/\Delta T)_{\text{PGW}}$. Here $(\Delta\alpha/\Delta T)_{\text{seasonal}}$ is calculated by differencing monthly mean values of α and T at adjacent months. Monthly differences are centered at the middle of each month to be most consistent with PGW values.

SAF-enhanced warming throughout the region. For example, [Bossert and Cotton \(1994\)](#) show terrain-forced diurnal flow regimes over the Headwaters region that include regional-scale upslope and downslope flows that may help ultimately determine the regional patterns and effects of the SAF. Furthermore, these wind systems themselves may be modulated by snow loss and the SAF. In addition, amplified nighttime warming in valleys and basins may relate to changes in nocturnal cold pools caused by changes in snow cover. Because snow cover increases cold pool strength by enhancing surface LW cooling (e.g., [Whiteman et al. 2001](#)), we expect weaker surface LW cooling in basins with substantial snow loss. Accordingly, snow cover loss may weaken nocturnal cold pools and facilitate more rapid cold pool destruction by convection during the day.

Energy transport was found to damp warming where the SAF was active ([Fig. 16](#)), enhance warming over nearby snow-free regions ([Fig. 5](#)), and enhance snowmelt over completely snow-covered regions ([Fig. 16](#)). These results have implications for experiments that force LSMs with surface meteorological conditions representative of possible future climate and are run in “offline” mode (e.g., [Elsner et al. 2010](#); [Vano et al. 2012](#)). In these experiments, the LSM-simulated surface conditions do not feedback into the forcing data. Thus, nonlocal effects of the SAF are not incorporated into the LSM forcing, since changes in surface albedo associated with snowmelt do not affect meteorological conditions elsewhere. Therefore, in regions where the SAF is relevant, these experiments may underestimate the rate of snowpack ablation, warming, and evapotranspiration.

There is a need for observational constraints on the SAF simulated by RCMs. The best way to observe

regional snow cover at high spatial resolution is through use of remote sensing platforms. Recent work performed by [Wrzesien et al. \(2015\)](#) used fractional snow cover estimated from MODIS satellite data using the MODIS Snow Covered-Area and Grain size retrieval algorithm (MODSCAG; [Painter et al. 2009](#)) to evaluate RCM simulations over the Sierra Nevada Mountains. They considered simulations using both the Noah LSM and the more sophisticated Noah-MP. While they found significant improvement in snowpack simulation using Noah-MP, both LSMs substantially overestimated f_{sn} over the Sierra Nevada. This bias will tend to lead to an overestimate of surface albedo in regions of snow cover and presumably would lead to an excessively large SAF in simulations of climate warming. More work is needed to characterize such biases and understand their implications for simulations of the SAF and regional climate warming.

5. Summary and conclusions

The aim of this study was to provide a better understanding of the snow albedo feedback (SAF) in simulations of regional climate change over the complex terrain of the Colorado Headwaters region. The SAF is most active throughout the spring months during the snow ablation season, when snow cover is particularly sensitive to temperature and when solar radiation is high. During the spring, spatial structures in warming are strongly correlated with snow loss, indicating a significant contribution from the SAF. Averaged over the Headwaters region, the enhancement of warming by the SAF may be as much as 1.5°C , with localized warming greater than 5°C . SAF-enhanced warming is most active

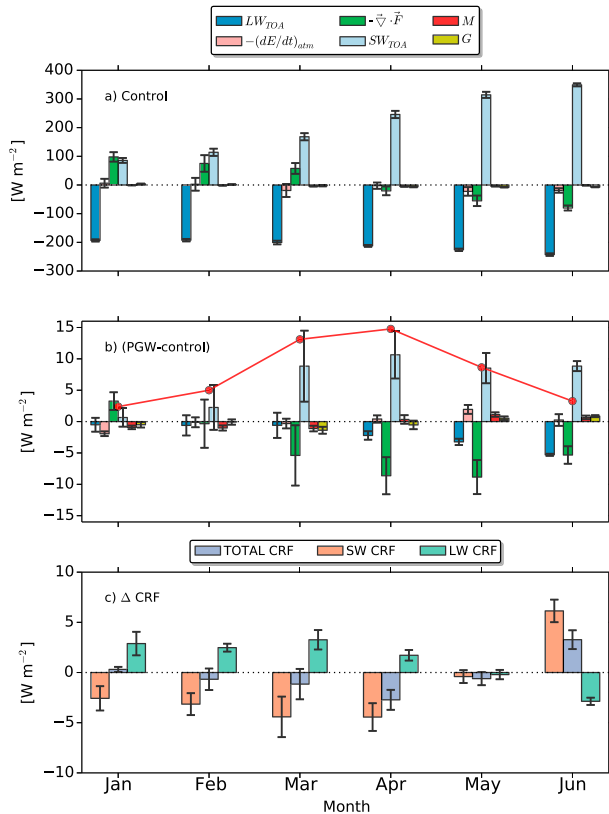


FIG. 15. Monthly mean terms of Eq. (8) averaged over the Headwaters region: (a) control, (b) (PGW-control), and (c) change in cloud radiative forcing (PGW-control). The solid red line in (b) represents the domain average $(\partial Q / \partial T_s)_{SAF}$ multiplied by ΔT_s . Whiskers represent interannual variability (± 1 standard deviation).

during the afternoon on the margins of the snowpack. Although this warming is generally reduced at night, it is pronounced overnight in valleys and basins. We speculate that this diurnal structure is due to regional-scale diurnal wind systems and changes in cold pool evolution. The SAF-enhanced warming is generally confined to the boundary layer but has increased vertical penetration along steep mountain slopes.

Linear feedback analysis was used to quantify the magnitude, seasonality, and the interannual variability of the SAF. The SAF is strongest during April with a mean of approximately $4 \text{ W m}^{-2} \text{ K}^{-1}$. There is high interannual variability in SAF strength within the Headwaters region, which is largely caused by interannual variability of regional snow cover. The SAF is strongest during high snowfall years because 1) more of the region is covered by snow, so the SAF is active over a larger area, and 2) snow cover persists later in the spring when incoming solar radiation is strong. The February–June average SAF strength is largely independent of variations in model grid spacing from $\Delta x = 4$ to 36 km.

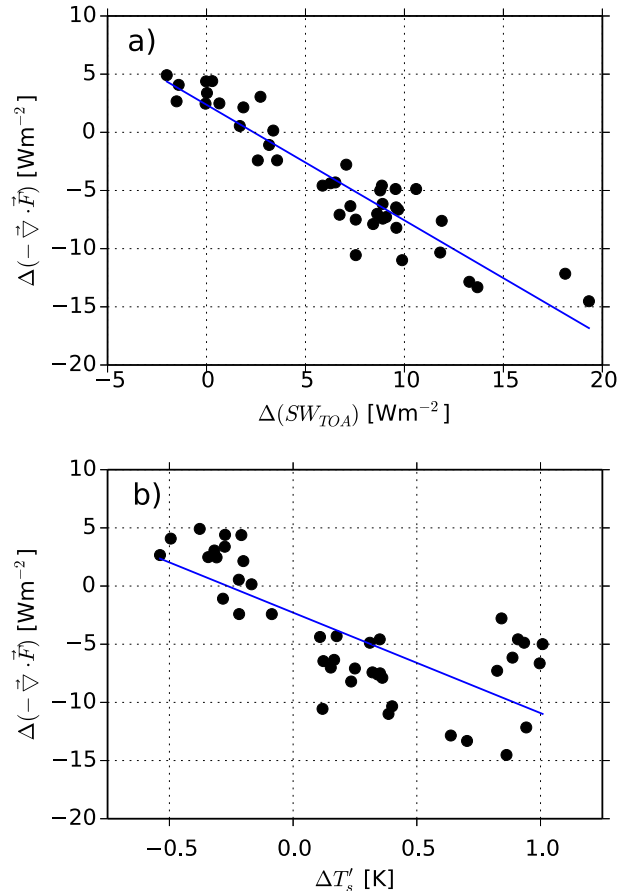


FIG. 16. Energy transport scattered against ΔSW_{TOA} and $\Delta T'_s$ for individual months January–June. The term $\Delta T'_s$ is ΔT_s minus ΔT_s averaged along the model boundaries. (a) ΔSW_{TOA} vs $\Delta(\mathbf{V} \cdot \mathbf{F})$ ($r = -0.93$, $p < 0.05$) and (b) $\Delta T'_s$ vs $\Delta(\mathbf{V} \cdot \mathbf{F})$ ($r = -0.74$, $p < 0.05$). Each point represents the Headwaters domain-average monthly mean value for a single year. The blue line shows the linear regression line.

However, on subseasonal scales, the SAF shows substantial resolution dependent differences in seasonality and spatial structure. At $\Delta x = 36$ -km, terrain smoothing homogenizes the climate, causing the SAF to reach its peak strength too early in the spring and to weaken too quickly into the late spring and summer months. It is possible that these differences are more substantial in coarser models, such as GCMs and many current RCMs.

The nonlocal effects of the SAF were investigated by examining changes in the atmospheric energy budget. The direct effect of the SAF is an increase in net SW radiative flux at the TOA. Energy transport by atmospheric circulations is the primary process that balances these SW changes. This transport facilitates nonlocal effects wherein the SAF enhances warming and snowmelt in locations that do not experience a loss of snow cover.

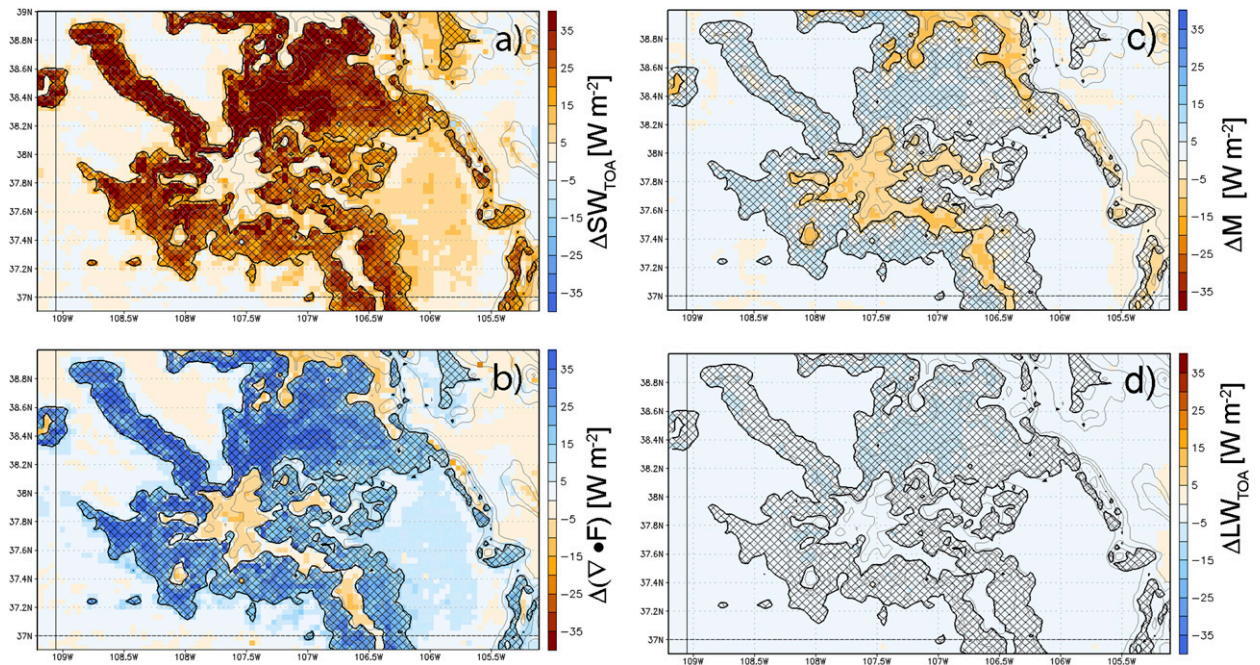


FIG. 17. Changes (PGW-control) in April energy flux terms from Eq. (8). Values are 7-yr averages (2002–08). (a) ΔSW_{TOA} , (b) $\Delta(\mathbf{V} \cdot \mathbf{F})$, (c) ΔM , and (d) ΔLW_{TOA} . Hatching indicates areas with >0.1 fractional snow loss. Light gray contours show the topography (interval of 200 m). Positive values indicate additional energy going into the atmospheric column.

The uniqueness and complexity of the regional terrain means that the specific results from this study cannot be directly applied to other mountain regions. Furthermore, the effects of snow impurities are not included in these simulations, and the SAF strength and timing may be substantially different in a model that includes these effects (e.g., Oaida et al. 2015). However, the methodological framework used here is generally applicable and can be used to diagnose the SAF in other RCM experiments and to help further the overall understanding of regional climate change in midlatitude mountain regions.

Acknowledgments. Support for this work was provided by the NSF Grant AGS-1349990. Initial work on this research was the result of a visit to NCAR by JRM funded by the NCAR Research Applications Lab visitors program. The NCAR Water System program funded by the NSF supported the generation of the RCM simulations analyzed here. We thank Kyoko Ikeda and Changhai Liu for providing assistance in accessing the RCM output and details of the model configuration. Roy Rasmussen provided helpful comments on an earlier version of the manuscript. High-performance computing support was provided by NCAR's Computational and Information Systems Laboratory, sponsored by the NSF. We are grateful to the anonymous

reviewers for their insightful comments and suggestions, which helped improve the quality of this paper.

REFERENCES

- Barlage, M., and Coauthors, 2010: Noah land surface model modifications to improve snowpack prediction in the Colorado Rocky Mountains. *J. Geophys. Res.*, **115**, D22101, doi:10.1029/2009JD013470.
- Bossert, J. E., and W. R. Cotton, 1994: Regional-scale flows in mountainous terrain. Part I: A numerical and observational comparison. *Mon. Wea. Rev.*, **122**, 1449–1471, doi:10.1175/1520-0493(1994)122<1449:RSFIMT>2.0.CO;2.
- Cess, R., and Coauthors, 1991: Interpretation of snow-climate feedback as produced by 17 general circulation models. *Science*, **253**, 888–892, doi:10.1126/science.253.5022.888.
- Chen, F., and J. Dudhia, 2001: Coupling an advanced land surface-hydrology model with the Penn State–NCAR MM5 modeling system. Part I: Model implementation and sensitivity. *Mon. Wea. Rev.*, **129**, 569–585, doi:10.1175/1520-0493(2001)129<0569:CAALSH>2.0.CO;2.
- , C. Liu, J. Dudhia, and M. Chen, 2014a: A sensitivity study of high-resolution regional climate simulations to three land surface models over the western United States. *J. Geophys. Res. Atmos.*, **119**, 7271–7291, doi:10.1002/2014JD021827.
- , and Coauthors, 2014b: Modeling seasonal snowpack evolution in the complex terrain and forested Colorado Headwaters region: A model intercomparison study. *J. Geophys. Res. Atmos.*, **119**, 13 795–13 819, doi:10.1002/2014JD022167.
- Christensen, N. S., and D. P. Lettenmaier, 2007: A multimodel ensemble approach to assessment of climate change impacts

- on the hydrology and water resources of the Colorado River Basin. *Hydrol. Earth Syst. Sci.*, **11**, 1417–1434, doi:[10.5194/hess-11-1417-2007](https://doi.org/10.5194/hess-11-1417-2007).
- , A. W. Wood, N. Voisin, D. P. Lettenmaier, and R. N. Palmer, 2004: The effects of climate change on the hydrology and water resources of the Colorado River basin. *Climatic Change*, **62**, 337–363, doi:[10.1023/B:CLIM.0000013684.13621.1f](https://doi.org/10.1023/B:CLIM.0000013684.13621.1f).
- Colman, R., 2003: A comparison of climate feedbacks in general circulation models. *Climate Dyn.*, **20**, 865–873, doi:[10.1007/s00382-003-0310-z](https://doi.org/10.1007/s00382-003-0310-z).
- Donohoe, A., and D. S. Battisti, 2011: Atmospheric and surface contributions to planetary albedo. *J. Climate*, **24**, 4402–4418, doi:[10.1175/2011JCLI3946.1](https://doi.org/10.1175/2011JCLI3946.1).
- Ek, M., K. Mitchell, Y. Lin, E. Rogers, P. Grunmann, V. Koren, G. Gayno, and J. Tarpley, 2003: Implementation of Noah land surface model advances in the National Centers for Environmental Prediction operational mesoscale Eta model. *J. Geophys. Res.*, **108**, 8851, doi:[10.1029/2002JD003296](https://doi.org/10.1029/2002JD003296).
- Elsner, M. M., and Coauthors, 2010: Implications of 21st century climate change for the hydrology of Washington State. *Climatic Change*, **102**, 225–260, doi:[10.1007/s10584-010-9855-0](https://doi.org/10.1007/s10584-010-9855-0).
- Feldl, N., and G. Roe, 2013a: Four perspectives on climate feedbacks. *Geophys. Res. Lett.*, **40**, 4007–4011, doi:[10.1002/grl.50711](https://doi.org/10.1002/grl.50711).
- , and —, 2013b: The nonlinear and nonlocal nature of climate feedbacks. *J. Climate*, **26**, 8289–8304, doi:[10.1175/JCLI-D-12-00631.1](https://doi.org/10.1175/JCLI-D-12-00631.1).
- Fernandes, R., H. Zhao, X. Wang, J. Key, X. Qu, and A. Hall, 2009: Controls on Northern Hemisphere snow albedo feedback quantified using satellite Earth observations. *Geophys. Res. Lett.*, **36**, L21702, doi:[10.1029/2009GL040057](https://doi.org/10.1029/2009GL040057).
- Fletcher, C. G., H. Zhao, P. J. Kushner, and R. Fernandes, 2012: Using models and satellite observations to evaluate the strength of snow albedo feedback. *J. Geophys. Res.*, **117**, D11117, doi:[10.1029/2012JD017724](https://doi.org/10.1029/2012JD017724).
- Fyfe, J. C., and G. M. Flato, 1999: Enhanced climate change and its detection over the Rocky Mountains. *J. Climate*, **12**, 230–243, doi:[10.1175/1520-0442-12.1.230](https://doi.org/10.1175/1520-0442-12.1.230).
- Gao, Y., J. A. Vano, C. Zhu, and D. P. Lettenmaier, 2011: Evaluating climate change over the Colorado River basin using regional climate models. *J. Geophys. Res.*, **116**, D13104, doi:[10.1029/2010JD015278](https://doi.org/10.1029/2010JD015278).
- Giorgi, F., J. W. Hurrell, M. R. Marinucci, and M. Beniston, 1997: Elevation dependency of the surface climate change signal: A model study. *J. Climate*, **10**, 288–296, doi:[10.1175/1520-0442\(1997\)010<0288:EDOTSC>2.0.CO;2](https://doi.org/10.1175/1520-0442(1997)010<0288:EDOTSC>2.0.CO;2).
- Hall, A., 2004: The role of surface albedo feedback in climate. *J. Climate*, **17**, 1550–1568, doi:[10.1175/1520-0442\(2004\)017<1550:TROSAF>2.0.CO;2](https://doi.org/10.1175/1520-0442(2004)017<1550:TROSAF>2.0.CO;2).
- , and X. Qu, 2006: Using the current seasonal cycle to constrain snow albedo feedback in future climate change. *Geophys. Res. Lett.*, **33**, L03502, doi:[10.1029/2005GL025127](https://doi.org/10.1029/2005GL025127).
- , —, and J. Neelin, 2008: Improving predictions of summer climate change in the United States. *Geophys. Res. Lett.*, **35**, L01702, doi:[10.1029/2007GL032012](https://doi.org/10.1029/2007GL032012).
- Ikeda, K., and Coauthors, 2010: Simulation of seasonal snowfall over Colorado. *Atmos. Res.*, **97**, 462–477, doi:[10.1016/j.atmosres.2010.04.010](https://doi.org/10.1016/j.atmosres.2010.04.010).
- Im, E.-S., E. Coppola, F. Giorgi, and X. Bi, 2010: Local effects of climate change over the alpine region: A study with a high resolution regional climate model with a surrogate climate change scenario. *Geophys. Res. Lett.*, **37**, L05704, doi:[10.1029/2009GL041801](https://doi.org/10.1029/2009GL041801).
- IPCC, 2000: *Emissions Scenarios*. Cambridge University Press, 570 pp.
- Kapnick, S., and A. Hall, 2012: Causes of recent changes in western North American snowpack. *Climate Dyn.*, **38**, 1885–1899, doi:[10.1007/s00382-011-1089-y](https://doi.org/10.1007/s00382-011-1089-y).
- Klos, P. Z., T. E. Link, and J. T. Abatzoglou, 2014: Extent of the rain-snow transition zone in the western U.S. under historic and projected climate. *Geophys. Res. Lett.*, **41**, 4560–4568, doi:[10.1002/2014GL060500](https://doi.org/10.1002/2014GL060500).
- Koren, V., J. Schaake, K. Mitchell, Q.-Y. Duan, F. Chen, and J. Baker, 1999: A parameterization of snowpack and frozen ground intended for NCEP weather and climate models. *J. Geophys. Res.*, **104**, 19 569–19 585, doi:[10.1029/1999JD900232](https://doi.org/10.1029/1999JD900232).
- Kotlarski, S., T. Bosshard, D. Lüthi, P. Pall, and C. Schär, 2012: Elevation gradients of European climate change in the regional climate model COSMO-CLM. *Climatic Change*, **112**, 189–215, doi:[10.1007/s10584-011-0195-5](https://doi.org/10.1007/s10584-011-0195-5).
- Leung, L. R., and Y. Qian, 2003: The sensitivity of precipitation and snowpack simulations to model resolution via nesting in regions of complex terrain. *J. Hydrometeorol.*, **4**, 1025–1043, doi:[10.1175/1525-7541\(2003\)004<1025:TSOPAS>2.0.CO;2](https://doi.org/10.1175/1525-7541(2003)004<1025:TSOPAS>2.0.CO;2).
- Mass, C. F., D. Ovens, K. Westrick, and B. A. Colle, 2002: Does increasing horizontal resolution produce more skillful forecasts? *Bull. Amer. Meteor. Soc.*, **83**, 407–430, doi:[10.1175/1520-0477\(2002\)083<0407:DIHRPM>2.3.CO;2](https://doi.org/10.1175/1520-0477(2002)083<0407:DIHRPM>2.3.CO;2).
- Merlis, T. M., 2014: Interacting components of the top-of-atmosphere energy balance affect changes in regional surface temperature. *Geophys. Res. Lett.*, **41**, 7291–7297, doi:[10.1002/2014GL061700](https://doi.org/10.1002/2014GL061700).
- Minder, J. R., D. R. Durran, and G. H. Roe, 2011: Mesoscale controls on the mountainside snow line. *J. Atmos. Sci.*, **68**, 2107–2127, doi:[10.1175/JAS-D-10-05006.1](https://doi.org/10.1175/JAS-D-10-05006.1).
- Mote, P. W., A. F. Hamlet, M. P. Clark, and D. P. Lettenmaier, 2005: Declining mountain snowpack in western North America. *Bull. Amer. Meteor. Soc.*, **86**, 39–49, doi:[10.1175/BAMS-86-1-39](https://doi.org/10.1175/BAMS-86-1-39).
- Nolin, A. W., and C. Daly, 2006: Mapping at risk snow in the Pacific Northwest. *J. Hydrometeorol.*, **7**, 1164–1171, doi:[10.1175/JHM543.1](https://doi.org/10.1175/JHM543.1).
- Oaida, C. M., Y. Xue, M. G. Flanner, S. M. Skiles, F. De Sales, and T. H. Painter, 2015: Improving snow albedo processes in wrf/ssib regional climate model to assess impact of dust and black carbon in snow on surface energy balance and hydrology over western U.S. *J. Geophys. Res. Atmos.*, **120**, 3228–3248, doi:[10.1002/2014JD022444](https://doi.org/10.1002/2014JD022444).
- Painter, T. H., A. P. Barrett, C. C. Landry, J. C. Neff, M. P. Cassidy, C. R. Lawrence, K. E. McBride, and G. L. Farmer, 2007: Impact of disturbed desert soils on duration of mountain snow cover. *Geophys. Res. Lett.*, **34**, L12502, doi:[10.1029/2007GL030284](https://doi.org/10.1029/2007GL030284).
- , K. Rittger, C. McKenzie, P. Slaughter, R. E. Davis, and J. Dozier, 2009: Retrieval of subpixel snow covered area, grain size, and albedo from MODIS. *Remote Sens. Environ.*, **113**, 868–879, doi:[10.1016/j.rse.2009.01.001](https://doi.org/10.1016/j.rse.2009.01.001).
- , J. S. Deems, J. Belnap, A. F. Hamlet, C. C. Landry, and B. Udall, 2010: Response of Colorado River runoff to dust radiative forcing in snow. *Proc. Natl. Acad. Sci. USA*, **107**, 17 125–17 130, doi:[10.1073/pnas.0913139107](https://doi.org/10.1073/pnas.0913139107).
- Pierce, D. W., and Coauthors, 2008: Attribution of declining western US snowpack to human effects. *J. Climate*, **21**, 6425–6444, doi:[10.1175/2008JCLI2405.1](https://doi.org/10.1175/2008JCLI2405.1).
- Porter, D. F., J. J. Cassano, and M. C. Serreze, 2011: Analysis of the Arctic atmospheric energy budget in WRF: A comparison with reanalyses and satellite observations. *J. Geophys. Res.*, **116**, D22108, doi:[10.1029/2011JD016622](https://doi.org/10.1029/2011JD016622).

- Qian, Y., M. Flanner, L. Leung, and W. Wang, 2011: Sensitivity studies on the impacts of Tibetan Plateau snowpack pollution on the Asian hydrological cycle and monsoon climate. *Atmos. Chem. Phys.*, **11**, 1929–1948, doi:10.5194/acp-11-1929-2011.
- Qu, X., and A. Hall, 2007: What controls the strength of snow-albedo feedback? *J. Climate*, **20**, 3971–3981, doi:10.1175/JCLI4186.1.
- , and —, 2014: On the persistent spread in snow-albedo feedback. *Climate Dyn.*, **42**, 69–81, doi:10.1007/s00382-013-1774-0.
- Randall, D. A., and Coauthors, 1994: Analysis of snow feedbacks in 14 general circulation models. *J. Geophys. Res.*, **99**, 20 757–20 771, doi:10.1029/94JD01633.
- Rasmussen, R., and Coauthors, 2011: High-resolution coupled climate runoff simulations of seasonal snowfall over Colorado: A process study of current and warmer climate. *J. Climate*, **24**, 3015–3048, doi:10.1175/2010JCLI3985.1.
- , and Coauthors, 2014: Climate change impacts on the water balance of the Colorado Headwaters: High-resolution regional climate model simulations. *J. Hydrometeorol.*, **15**, 1091–1116, doi:10.1175/JHM-D-13-0118.1.
- Roe, G., 2009: Feedbacks, timescales, and seeing red. *Annu. Rev. Earth Planet. Sci.*, **37**, 93–115, doi:10.1146/annurev.earth.061008.134734.
- Salathé, E. P., Jr., R. Steed, C. F. Mass, and P. H. Zahn, 2008: A high-resolution climate model for the U.S. Pacific Northwest: Mesoscale feedbacks and local responses to climate change. *J. Climate*, **21**, 5708–5726, doi:10.1175/2008JCLI2090.1.
- Schär, C., C. Frei, D. Lüthi, and H. C. Davies, 1996: Surrogate climate-change scenarios for regional climate models. *Geophys. Res. Lett.*, **23**, 669–672, doi:10.1029/96GL00265.
- Skamarock, W., and Coauthors, 2008: A description of the Advanced Research WRF version 3. NCAR Tech. Note NCAR/TN-475+STR, 113 pp. [Available online at http://www.mmm.ucar.edu/wrf/users/docs/arw_v3_bw.pdf.]
- Soden, B. J., I. M. Held, R. Colman, K. M. Shell, J. T. Kiehl, and C. A. Shields, 2008: Quantifying climate feedbacks using radiative kernels. *J. Climate*, **21**, 3504–3520, doi:10.1175/2007JCLI2110.1.
- Taylor, K., M. Crucifix, P. Braconnot, C. Hewitt, C. Doutriaux, A. Broccoli, J. Mitchell, and M. Webb, 2007: Estimating shortwave radiative forcing and response in climate models. *J. Climate*, **20**, 2530–2543, doi:10.1175/JCLI4143.1.
- Trenberth, K., J. Caron, and D. Stepaniak, 2001: The atmospheric energy budget and implications for surface fluxes and ocean heat transports. *Climate Dyn.*, **17**, 259–276, doi:10.1007/PL00007927.
- Vano, J. A., T. Das, and D. P. Lettenmaier, 2012: Hydrologic sensitivities of Colorado River runoff to changes in precipitation and temperature. *J. Hydrometeorol.*, **13**, 932–949, doi:10.1175/JHM-D-11-069.1.
- Whiteman, C. D., S. Zhong, W. J. Shaw, J. M. Hubbe, X. Bian, and J. Mittelstadt, 2001: Cold pools in the Columbia Basin. *Wea. Forecasting*, **16**, 432–447, doi:10.1175/1520-0434(2001)016<0432:CPITCB>2.0.CO;2.
- Wigmosta, M. S., L. W. Vail, and D. P. Lettenmaier, 1994: A distributed hydrology-vegetation model for complex terrain. *Water Resour. Res.*, **30**, 1665–1680, doi:10.1029/94WR00436.
- Wrzesien, M. L., T. M. Pavelsky, S. B. Kapnick, M. T. Durand, and T. H. Painter, 2015: Evaluation of snow cover fraction for regional climate simulations in the Sierra Nevada. *Int. J. Climatol.*, **35**, 2472–2484, doi:10.1002/joc.4136.